IEEE Open Journal of
Power Electronics

Received 13 May 2026; revised 4 June 2026; accepted 6 June 2026. Date of publication 11 June 2026;
date of current version 15 July 2026. The review of this article was arranged by Associate Editor Satish Naik Banavath.

Digital Object Identifier 10.1109/OJPEL.2026.3702573

A General Analysis of Passive Component Sizing for Current-Sourced Buck Converters

QIJIA LI (Graduate Student Member, IEEE), JONAH RAWLEY (Graduate Student Member, IEEE), AND SAMANTHA CODAY (Member, IEEE)

Department of Electrical Engineering and Computer Science, Massachusetts Institute of Technology, Cambridge, MA 02139 USA

CORRESPONDING AUTHOR: Qijia Li (e-mail: qijia268@mit.edu)

ABSTRACT Power converter topologies with inductors at the input offer the potential to reduce conducted electromagnetic interference (EMI). To harness this benefit in converters conventionally implemented with inductors at the output, an input passive network consisting of two inductors and a bypass capacitor can be utilized instead of the output inductor. This work focuses on the current-sourced buck converter (CSBC), the most fundamental two input inductor topology, and presents a comprehensive analytical model for the bypass capacitor voltage and input inductor currents. In addition, an analytical expression for the output voltage is derived, demonstrating its dependence on not only the duty ratio but also the switching and resonant frequencies of the CSBC. The analysis is expanded from an uncoupled CSBC to include magnetic coupling between the input inductors, which enables the CSBC to be implemented with only one magnetic core. The effects of coupling are thoroughly analyzed, including the potential to reduce passive component volume. The proposed model is validated through simulation and experimental results for a design example. Design insights are provided to guide passive component value selection, evaluate switch stress based on capacitor voltage and inductor current ripples, and identify operating conditions where magnetic coupling may be beneficial in reducing passive component volume.

INDEX TERMS Input inductor buck converter, current-sourced buck converter.

I. INTRODUCTION

This work presents a general analysis of component sizing for the CSBC [1], shown in Fig. 1, a topology which has also been referred to as the input inductor buck converter [2], [3], current-type buck converter [4], [5], [6], two inductor buck converter [7], Kappa converter [8], third-order buck converter [9], and superbuck converter [10], [11]. While the CSBC nominally provides the same conversion ratio as a conventional buck converter, the placement of the inductors at the input of the converter alters its functionality, presenting advantages and disadvantages. Two inductors are required, which increases part count and design complexity compared to a conventional buck converter. Furthermore, splitting the converter's magnetic energy storage requirements between two inductors generally results in larger overall component volume due to the scaling properties of magnetic components [12]. Component integration can be improved by magnetically coupling the two inductors, but this

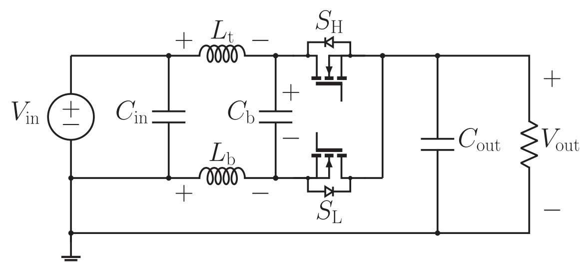

FIGURE 1. Schematic of the CSBC implemented with two uncoupled inductors.

further complicates magnetic design and introduces fundamental tradeoffs in the sizing of the input passive components, which are explored in this work. At the same time, the input inductors enforce a continuous input current, a significant benefit which has been exploited in various applications, such as photovoltaic power conversion where continuous input current is beneficial for maximum power point tracking algorithms [11]. In contrast to standard current-sourced topologies such as the boost converter or SEPIC converter, the CSBC can be designed to have no RHP zero, thereby improving controller bandwidth [1].

More recently, interest in multilevel topologies utilizing the input passive network of the CSBC have been explored for various applications. Continuous current draw at the input has the potential to reduce conducted EMI [8], which is exploited in the development of the input inductor power factor correction (PFC) converter in [3]. In addition, recent studies have demonstrated that current-sourced hybrid switched-capacitor converters (SCCs) enable high power density [13] and provide a foundation for future system-in-package (SiP) and system-on-chip (SoC) implementations [5], [6]. These features directly address the design criteria for point-of-load (PoL) converters in data centers, which prioritize high power delivery capability and compact size [14], thereby positioning current-sourced converters as a potentially competitive candidate for such applications. Furthermore, the adoption of the two inductor input passive network has facilitated the development of novel converter topologies, including the condensed buck-boost (CoBB) converter [15], which improves multilevel scaling in applications requiring both buck and boost functionality.

Although interest in current-sourced converter topologies based on the two inductor input passive network continues to rise, limited research has been conducted on the bypass capacitor (C_b in Fig. 1). Prior studies on CSBCs commonly adopt a linear model for voltage and current ripple calculation, in which simplifying assumptions are applied to evaluate the behavior of inductors and the capacitor [1], [7], [10], [11]. Specifically, when calculating the input inductor current ripples, the bypass capacitor voltage ripple is neglected, leading to the assumption of linear inductor current waveforms and yielding an output voltage of $V_\mathrm{out} = DV_\mathrm{in}$. Conversely, to obtain the C_b voltage ripple, the inductor current ripples are assumed negligible, resulting in a linear capacitor voltage waveform. Using these linear assumptions, for a given switching period (T_sw) and a load resistance (R_load), the voltage and current ripples are calculated as

$$\Delta i_\mathrm{n} = \frac{(V_\mathrm{in} - V_\mathrm{out})DT_\mathrm{sw}}{L_\mathrm{n}}, \quad \mathrm{n} \in \{\mathrm{t,b}\} \tag{1}$$

$$\Delta v_{C_\mathrm{b}} = \frac{V_\mathrm{out}(1-D)DT_\mathrm{sw}}{R_\mathrm{load}C_\mathrm{b}}, \tag{2}$$

where Δi_t, Δi_b, and Δv_{C_b} denote the peak-to-peak inductor current ripples and capacitor voltage ripple respectively.

While this linear model simplifies analysis and provides general design guidelines, its underlying assumptions inherently decouple the ripple effects of the inductors and capacitor. As a result, the capacitor voltage ripple and inductor current ripple are not simultaneously captured within a unified framework. This linear model has two main sources of inaccuracy. First, it assumes that the output voltage is always DV_in, which is not the case in practice when both capacitor voltage ripple and inductor current ripples are included. Any error in the output voltage approximation further propagates into the linear model equations shown in (1) and (2). Second, it only considers the linear ripple and therefore neglects ripple components which occur due to resonance in the input passive network. As shown in Fig. 2, the shape and peak-to-peak ripples of the linear model waveforms exhibit significant disagreement with simulated results. The limitations of the linear model therefore necessitate conservative over-design of the passive components to ensure that the specified ripple constraints are satisfied in practice. Moreover, the uncharacterized capacitor voltage ripple can lead to non-optimal design choices for other components, such as switches, whose voltage and current stresses are directly influenced by these ripple magnitudes. To address these limitations and reduce the total passive component volume, a more accurate model is proposed in this work. The comparison between the linear and proposed models under the same resonant frequency f_res and varying switching frequency f_sw shown in Fig. 2 demonstrates the improved accuracy of the proposed model. The development of the proposed model along with a detailed discussion of the limitations of the linear model will be presented in the following sections.

This work is an extension of [2] and presents a comprehensive model of the CSBC. Beyond analytical accuracy, the proposed model provides practical design insights by relating switching frequency, power level, load condition, and passive component sizing to the resulting capacitor voltage and inductor current ripples. In addition, though the potential to improve magnetic component integration by coupling has been noted in literature [1], [11], its effects have not been explored in depth. This work provides a detailed analysis of the effect of coupling on the passive component waveforms and their required volumes, denoting uncoupled and coupled inductor implementations respectively as U-CSBC and C-CSBC. The developed model enables designers to quantitatively evaluate whether the capacitor voltage ripple and inductor current ripples satisfy given design constraints and, more importantly, to systematically select appropriate inductance and capacitance values to achieve desired ripple performance and minimized passive component volume.

The major contributions of this work are summarized as follows:

- A comprehensive analysis of the U-CSBC is developed in Section II, where general expressions for the bypass capacitor voltage, output voltage, and input inductor currents are derived which remain applicable under varying conditions. The developed analysis is then extended to the C-CSBC in Section III.
- A thorough discussion on the implications of coupling the input inductors, including its effects on passive component volume and other practical design considerations, is presented in Section IV.

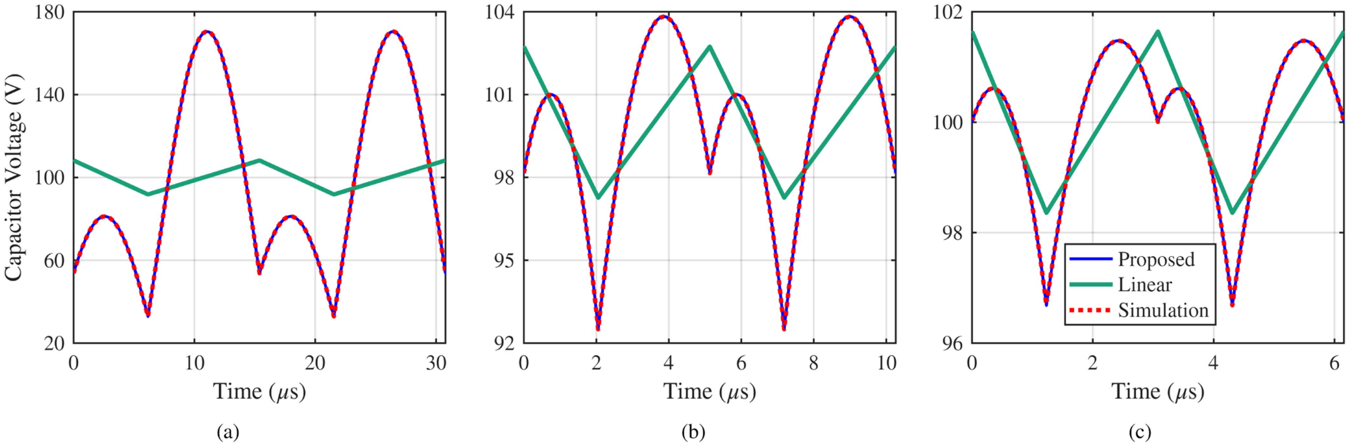

FIGURE 2. Capacitor voltage waveforms obtained from the linear and proposed models compared with simulations. The values of passive components are $L_t = L_b = 30\ \mu$H and $C_b = 0.2\ \mu$F. The operating conditions are $V_{in} = 100$ V, $D = 0.4$, and $R_{load} = 45\ \Omega$. (a) $f_{sw} = f_{res}$; (b) $f_{sw} = 3f_{res}$; (c) $f_{sw} = 5f_{res}$.

- A design example for U-CSBCs and C-CSBCs is presented in Section V, demonstrating that the developed model enables improved component selection compared to the conventional linear approach. Experimental validation is provided in Section VI.
- A comparison between the CSBC and conventional buck converters based on the equivalence between coupled input inductors and conventional output inductance is derived in Appendix A and B.

The analysis presented in this work establishes a foundation for extending the developed methodology to other topologies incorporating input inductors, thereby supporting future optimization of current-sourced converters for a wide range of applications.

II. THEORETICAL ANALYSIS OF THE U-CSBC

In this section, analytical expressions for the bypass capacitor voltage and input inductor currents for the uncoupled case are derived. These expressions form the basis for voltage and current ripple analysis associated with switch stress and for evaluation of potential passive component volume reduction. For simplification of the model, the ripple of the output voltage is assumed to be negligible such that the output voltage is a constant, V_{out}. The focus of this work is primarily on passive component volume, and as such, losses are excluded to reduce complexity and generalize the analysis. However, as the converter losses are dependent on the passive component waveforms, the developed model can be applied to analyze the influence of component selection on efficiency. Additionally, the proposed modeling approach can be extended to explicitly include losses which presents a compelling direction for future work.

The voltage across the bypass capacitor is represented as a time-dependent function, $v_{C_b}(t)$. Moreover, two-phase operation is assumed for the CSBC, and the converter's behavior in each phase is analyzed separately in the following two subsections.

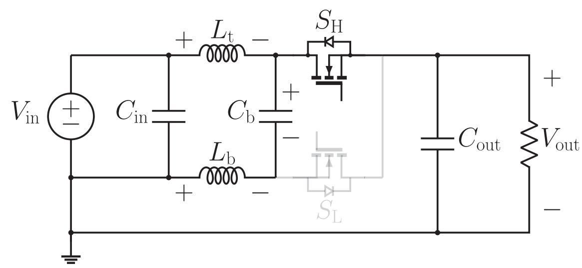

FIGURE 3. Phase one operation of the U-CSBC.

A. PHASE ONE

When S_H is conducting, as shown in Fig. 3, the inductor voltages can be expressed using Kirchhoff's Voltage Law (KVL) as

$$V_{L_t,1} = V_{in} - V_{out} \tag{3}$$

$$v_{L_b,1}(t) = v_{C_b,1}(t) - V_{out}. \tag{4}$$

Since the current through the bottom inductor, $i_{L_b}(t)$, flows only into C_b during phase one, $i_{L_b,1}(t) = -i_{C_b,1}(t)$. The constitutive equation of a capacitor describes the current flowing through the bypass capacitor, $i_{C_b}(t)$, in terms of $v_{C_b}(t)$. Thus, the voltage across the bottom inductor can also be expressed as

$$\begin{aligned} v_{L_b,1}(t) &= L_b \frac{di_{L_b,1}(t)}{dt} \\ &= -L_b \frac{di_{C_b,1}(t)}{dt} \\ &= -C_b L_b \frac{d^2 v_{C_b,1}(t)}{dt^2}. \end{aligned} \tag{5}$$

Combining (4) and (5) yields

$$C_b L_b \frac{d^2 v_{C_b,1}(t)}{dt^2} + v_{C_b,1}(t) - V_{out} = 0. \tag{6}$$

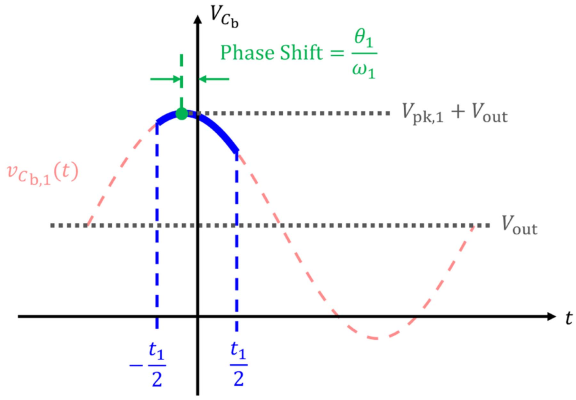

FIGURE 4. A visualization of $v_{C_b,1}(t)$.

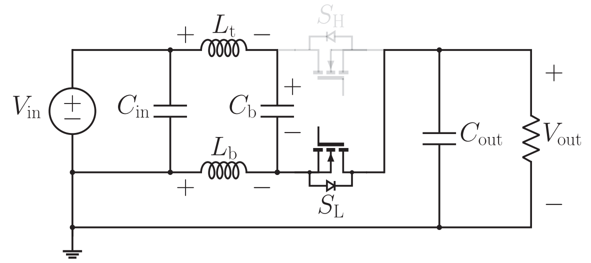

FIGURE 5. Phase two operation of the U-CSBC.

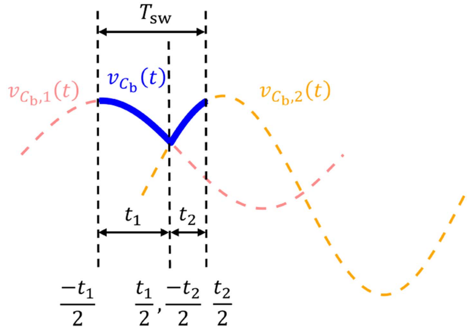

FIGURE 6. The bypass capacitor voltage waveform over a period. As shown, $v_{C_b}(t)$ is the combination of the waveforms of two states, $v_{C_b,1}(t)$ and $v_{C_b,2}(t)$.

This second-order linear ordinary differential equation can be solved as in (7), with free parameters A and B

$$v_{C_b,1}(t) = \sqrt{A^2 + B^2} \cos\left(\frac{1}{\sqrt{C_b L_b}} t - \tan^{-1}\left(\frac{B}{A}\right)\right) + V_{out}. \tag{7}$$

Thus, the general behavior of the bypass capacitor voltage can be described by a cosine function. To simplify the expression, $V_{pk,1}$ is introduced to represent the amplitude of the cosine waveform, and θ_1 represents the phase shift,

$$v_{C_b,1}(t) = V_{pk,1} \cos\left(\frac{1}{\sqrt{C_b L_b}} t + \theta_1\right) + V_{out}. \tag{8}$$

In phase one, the voltage across the top inductor remains constant according to (3), allowing the inductor to be modeled as an ac short. As a result, L_t does not contribute to the resonant frequency in this phase, and the circuit reduces to an LC tank formed solely by C_b and L_b. The resulting resonant frequency of phase one is $\omega_1 = 1/\sqrt{C_b L_b}$, which is consistent with the resonant frequency found in (8).

With phase durations defined as

$$t_1 = DT_{sw}, \ t_2 = (1 - D)T_{sw}, \tag{9}$$

the bypass capacitor waveform for phase one can be represented as a segment of length t_1 extracted from $v_{C_b,1}(t)$ waveform, as illustrated in Fig. 4. Here, $V_{pk,1}$ is assumed to be positive for clearer visualization. It should be noted, however, that $V_{pk,1}$ may in general be either positive or negative. As $v_{C_b,1}(t)$ is a cosine function with amplitude $V_{pk,1}$, any sign change in $V_{pk,1}$ is mathematically equivalent to a shift in the phase θ_1 and does not affect the waveform shape. In addition, the time interval of phase one is chosen to be $[-\frac{t_1}{2}, \frac{t_1}{2}]$ to simplify the calculation.

The inductor current expressions are derived as follows. During this phase, $i_{L_t,1}(t)$ varies linearly because the inductor voltage $V_{L_t,1}$ is constant. By continuity of inductor current, the initial value of $i_{L_t,1}(t)$ equals the final value of $i_{L_t,2}(t)$, which is $i_{L_t,2}(\frac{t_2}{2})$. For the bottom inductor, $i_{L_b,1}(t) = -i_{C_b,1}(t)$, which can be derived by differentiating (8). The resulting expressions are summarized in Table 1.

B. PHASE TWO

Following the same method, during phase two, as shown in Fig. 5, the bypass capacitor voltage can be expressed as

$$v_{C_b,2}(t) = V_{pk,2} \cos\left(\frac{1}{\sqrt{C_b L_t}} t + \theta_2\right) + V_{in} - V_{out}, \tag{10}$$

where the respective resonant frequency is given by $\omega_2 = 1/\sqrt{C_b L_t}$. In this phase, $V_{L_b,2} = -V_{out}$ and $v_{L_t,2}(t) = V_{in} - V_{out} - v_{C_b,2}(t)$. The per-phase inductor current expressions are listed in Table 1 and the time interval of phase two is $[-\frac{t_2}{2}, \frac{t_2}{2}]$ correspondingly.

The overall behavior of $v_{C_b}(t)$ can be described as the piecewise combination of $v_{C_b,1}(t)$ and $v_{C_b,2}(t)$ waveforms over a period as depicted in Fig. 6. A similar piecewise formulation also applies to the inductor current waveforms due to continuity. The amplitudes of the cosine expressions (8), (10), $V_{pk,1}$ and $V_{pk,2}$, along with the corresponding phase shifts, θ_1 and θ_2, will be discussed in the next subsection.

C. DERIVATION OF EQUATIONS

To determine the capacitor voltage and inductor currents in both phases, the five unknowns ($V_{pk,1}$, $V_{pk,2}$, θ_1, θ_2, and V_{out}) must be found utilizing five equations derived from the topology. For the following analysis, $V_{pk,1}$ and $V_{pk,2}$ are assumed to be positive, and θ_1 and θ_2 are calculated correspondingly.

TABLE 1. Derived Expressions for Voltages and Currents in U-CSBCs

	Phase One $[-\frac{t_1}{2}, \frac{t_1}{2}]$	Phase Two $[-\frac{t_2}{2}, \frac{t_2}{2}]$
$v_{L_t}(t)$	$V_{in} - V_{out}$	$-V_{pk,2}\cos(\omega_2 t + \theta_2)$
$v_{L_b}(t)$	$V_{pk,1}\cos(\omega_1 t + \theta_1)$	$-V_{out}$
$v_{C_b}(t)$	$V_{pk,1}\cos(\omega_1 t + \theta_1) + V_{out}$	$V_{pk,2}\cos(\omega_2 t + \theta_2) + V_{in} - V_{out}$
$i_{C_b}(t)$	$-V_{pk,1}C_b\omega_1\sin(\omega_1 t + \theta_1)$	$-V_{pk,2}C_b\omega_2\sin(\omega_2 t + \theta_2)$
$i_{L_t}(t)$	$i_{L_t,2}(\frac{t_2}{2}) + \frac{V_{in}-V_{out}}{L_t}(t + \frac{t_1}{2})$	$-V_{pk,2}C_b\omega_2\sin(\omega_2 t + \theta_2)$
$i_{L_b}(t)$	$V_{pk,1}C_b\omega_1\sin(\omega_1 t + \theta_1)$	$i_{L_b,1}(\frac{t_1}{2}) + \frac{-V_{out}}{L_b}(t + \frac{t_2}{2})$

For the cases of interest investigated in this paper, when I_{out} is positive and $v_{C_b}(t)$ is always larger than zero, C_b is predominantly discharged during phase one and $v_{C_{b,1}}(t)$ exhibits a net decrease, whereas in phase two, C_b is predominantly charged and $v_{C_{b,2}}(t)$ shows an overall rising trend. Consequently, the minimum value of $v_{C_b}(t)$ over one switching period always occurs at the transition from phase one to phase two. According to (8) and (10), and noting that $V_{pk,1} > 0$ and $V_{pk,2} > 0$, $v_{C_{b,1}}(t)$ must be shifted toward negative time and $v_{C_{b,2}}(t)$ shifted toward positive time so that the transition point corresponds to the minimum of the waveform. This requirement leads to $\theta_1 > 0$ and $\theta_2 < 0$.

Based on the periodic steady-state analysis, the average voltage across an inductor over a switching period is zero, which directly yields one volt-second balance equation for each input inductor. The simplified volt-second balance equations for L_t and L_b respectively are

$$\frac{2V_{pk,2}}{\omega_2}\sin\left(\omega_2\frac{t_2}{2}\right)\cos(\theta_2) = (V_{in} - V_{out})t_1 \tag{11}$$

$$\frac{2V_{pk,1}}{\omega_1}\sin\left(\omega_1\frac{t_1}{2}\right)\cos(\theta_1) = V_{out}t_2. \tag{12}$$

From these two equations, it follows that $0 < \theta_1 < \frac{\pi}{2}$ and $-\frac{\pi}{2} < \theta_2 < 0$. Additionally, the voltage continuity of $v_{C_b}(t)$ at the phase boundaries leads to

$$V_{pk,1}\cos\left(\omega_1\frac{t_1}{2} + \theta_1\right) + V_{out} = V_{pk,2}\cos\left(\omega_2\frac{-t_2}{2} + \theta_2\right) + V_{in} - V_{out} \tag{13}$$

$$V_{pk,1}\cos\left(\omega_1\frac{-t_1}{2} + \theta_1\right) + V_{out} = V_{pk,2}\cos\left(\omega_2\frac{t_2}{2} + \theta_2\right) + V_{in} - V_{out}. \tag{14}$$

As V_{out} is assumed to be constant, the average output current I_{out} is correspondingly constant. The instantaneous output current equals the sum of the two inductor currents for both phases, $i_{out}(t) = i_{L_t}(t) + i_{L_b}(t)$, and therefore the average output current can be expressed as

$$I_{out} = \frac{1}{T}\left(\int_{\frac{-t_1}{2}}^{\frac{t_1}{2}} i_{out,1}(t)\,dt + \int_{\frac{-t_2}{2}}^{\frac{t_2}{2}} i_{out,2}(t)\,dt\right) = \frac{1}{T}(I_1 + I_2), \tag{15}$$

where I_1 and I_2 are parameters defined as follows:

$$I_1 = \frac{V_{in} - V_{out}}{2L_t}{t_1}^2 - V_{pk,2}C_b\omega_2 t_1\sin\left(\omega_2\frac{t_2}{2} + \theta_2\right) + 2V_{pk,1}C_b\sin\left(\omega_1\frac{t_1}{2}\right)\sin(\theta_1) \tag{16}$$

$$I_2 = \frac{-V_{out}}{2L_b}{t_2}^2 + V_{pk,1}C_b\omega_1 t_2\sin\left(\omega_1\frac{t_1}{2} + \theta_1\right) - 2V_{pk,2}C_b\sin\left(\omega_2\frac{t_2}{2}\right)\sin(\theta_2). \tag{17}$$

In summary, five equations (11)–(15) are derived that can be used to solve for five unknowns: $V_{pk,1}$, $V_{pk,2}$, θ_1, θ_2, and V_{out}. Given designer-selected values for input voltage, output load, passive component values, duty ratio, and switching frequency, exact analytical expressions for the bypass capacitor voltage and inductor currents can then be obtained.

D. OUTPUT VOLTAGE

If the inductor currents are assumed to be linear, the output voltage can be expressed as $V_{out} = DV_{in}$. However, by combining (11)–(14), this work derives the analytical expression to provide an exact calculation of the output voltage as

$$V_{out} = V_{in}\frac{\frac{t_1\omega_2}{\tan(\omega_2\frac{t_2}{2})} + 2}{\frac{t_2\omega_1}{\tan(\omega_1\frac{t_1}{2})} + \frac{t_1\omega_2}{\tan(\omega_2\frac{t_2}{2})} + 4}. \tag{18}$$

This suggests that V_{out} is a function of the two resonant frequencies, the switching frequency, and the duty ratio given in (9). To quantify the extent to which the switching frequency is greater than the resonant frequency, two parameters, Γ_1 and Γ_2, are defined as

$$\Gamma_1 = \frac{\omega_{\mathrm{sw}}}{\omega_1} = \omega_{\mathrm{sw}}\sqrt{L_{\mathrm{b}}C_{\mathrm{b}}} \tag{19}$$

$$\Gamma_2 = \frac{\omega_{\mathrm{sw}}}{\omega_2} = \omega_{\mathrm{sw}}\sqrt{L_{\mathrm{t}}C_{\mathrm{b}}}. \tag{20}$$

Combining (18)–(20) leads to

$$V_{\mathrm{out}} = V_{\mathrm{in}} \frac{\dfrac{\frac{2\pi D}{\Gamma_2}}{\tan\left(\frac{\pi(1-D)}{\Gamma_2}\right)} + 2}{\dfrac{\frac{2\pi(1-D)}{\Gamma_1}}{\tan(\frac{\pi D}{\Gamma_1})} + \dfrac{\frac{2\pi D}{\Gamma_2}}{\tan\left(\frac{\pi(1-D)}{\Gamma_2}\right)} + 4}. \tag{21}$$

In the special cases where $\Gamma_1 = \Gamma_2$ and $D = 1/2$, (21) is equivalent to $V_{\mathrm{out}} = DV_{\mathrm{in}}$. However, V_{out} is more accurately determined by the interdependence of Γ_1, Γ_2, and the duty ratio. As depicted in Fig. 7(a), when $D = 1/4$, densely packed contour lines are observed in the region where Γ_1 and Γ_2 are relatively small, indicating that slight variations in the resonant frequencies result in large changes in the output voltage. Notably, the dense contour lines appear approximately horizontal, suggesting that changes in Γ_2 have a more pronounced effect on the output voltage than the changes in Γ_1. As both Γ_1 and Γ_2 become sufficiently large, (21) converges to DV_{in}. A similar analysis can be conducted for the cases shown in Fig. 7(b) and (c), which correspond to a duty ratio of 1/2 and 3/4 respectively.

Fig. 7 shows that, to obtain an output voltage close to DV_{in} and to ensure low sensitivity to variations in Γ_1 and Γ_2 (i.e., to operate in a region where the contour lines are sparse), the minimum of these two parameters, defined as

$$\Gamma_{\min} = \min\{\Gamma_1, \Gamma_2\}, \tag{22}$$

must be sufficiently large to satisfy specific output voltage regulation requirements. Accordingly, there exists a fundamental tradeoff between the switching frequency and passive component sizing. Higher switching frequency permits the use of smaller inductance and capacitance values while increasing switching losses, whereas larger inductance and capacitance values lower the resonant frequency and reduce switching losses at the cost of increased passive component volume.

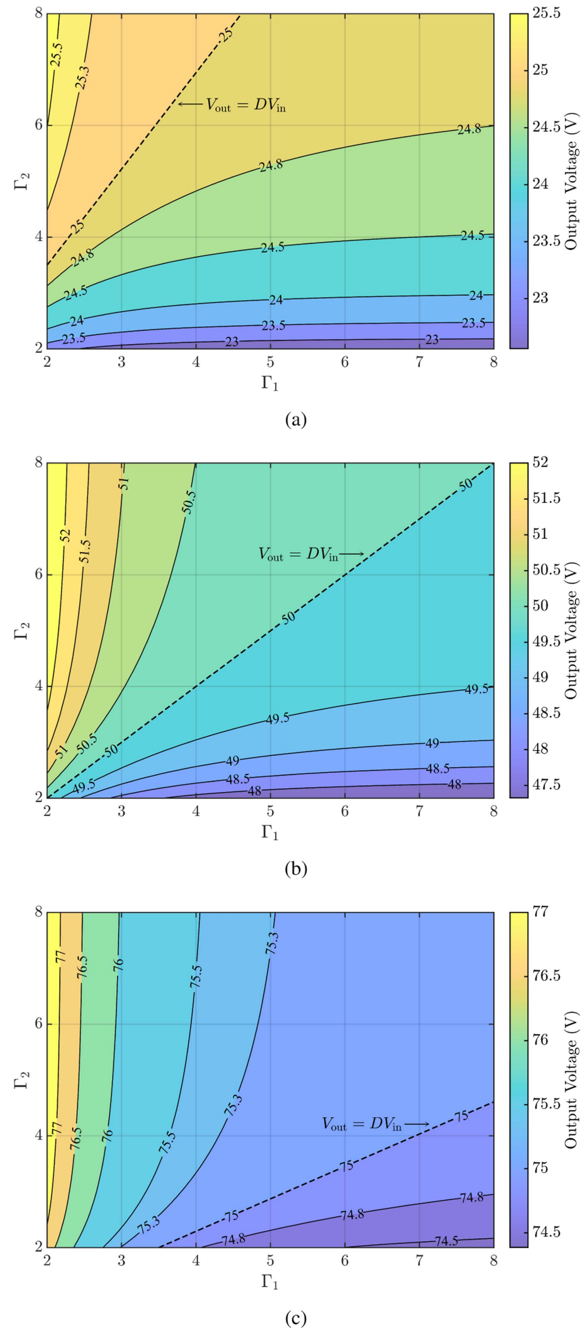

FIGURE 7. Modeled variation in output voltage as a function of Γ_1 and Γ_2. $V_{\mathrm{in}} = 100$ V. The duty ratios are: (a) $D = 1/4$, (b) $D = 1/2$, and (c) $D = 3/4$.

E. BYPASS CAPACITOR VOLTAGE RIPPLE

Although the average bypass capacitor voltage is equal to V_{in}, the voltage ripple varies across different operating conditions. Since the capacitor voltage influences the energy storage of passive components and thereby their sizing requirements, as well as the peak voltage stress across the switches, a careful analysis of the voltage ripple is essential to support optimal component choices.

The peak-to-peak capacitor voltage ripple can be determined as the difference between its maximum and minimum values. The minimum capacitor voltage occurs at the transition from phase one to phase two. The maximum voltage, however, needs to be found based on specific operating conditions. Since the bypass capacitor voltage waveform is comprised of segments from two cosine functions corresponding to the two operating states, whether each segment contains the cosine peak or not determines the location of the maximum value. Specifically, if a segment contains a cosine peak, the capacitor voltage waveform in that state exhibits non-monotonic behavior, implying that the maximum value of the segment occurs at the peak. Conversely, if no peak is present, the waveform of that state is monotonic and the maximum value occurs at the endpoint. Since there are two states and

TABLE 2. **Different Cases of the Bypass Capacitor Voltage Ripple**

	Case 1	Case 2	Case 3	Case 4
Phase One	Monotonic	Non-Monotonic	Monotonic	Non-Monotonic
Phase Two	Monotonic	Monotonic	Non-Monotonic	Non-Monotonic
Waveforms		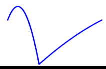	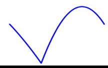	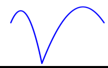

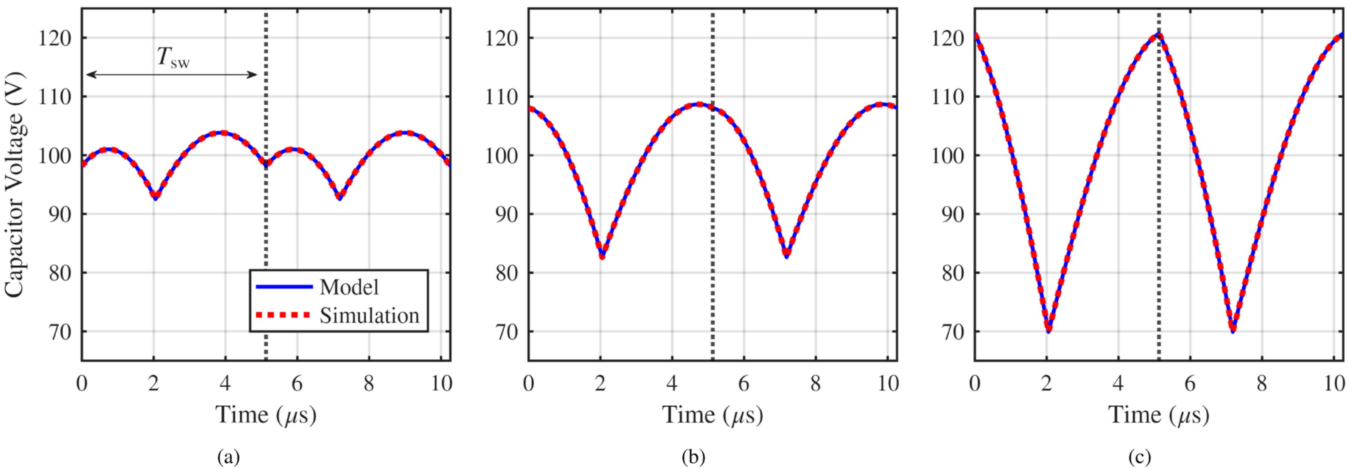

FIGURE 8. **Calculated and simulated capacitor voltage waveforms under three different output powers. The values of passive components are $L_t = L_b =$ 30 μH and $C_b = 0.2$ μF. The operating conditions are $V_{in} = 100$ V, $D = 0.4$, and $f_{sw} = 3f_{res}$. The case numbers (as defined in Table 2), output loads, and power levels are: (a) Case 4: $R_{load} = 45$ Ω, $P_{out} \approx 36$ W; (b) Case 3: $R_{load} = 10$ Ω, $P_{out} \approx 160$ W; (c) Case 1: $R_{load} = 5$ Ω, $P_{out} \approx 320$ W.**

the behavior of each state needs to be considered, there are four potential cases as shown in Table 2.

Although an accurate evaluation of the bypass capacitor voltage ripple requires detailed analysis, its overall variation trend can be examined qualitatively. For instance, Fig. 8 shows how the capacitor voltage ripple varies with output power. Since $\Gamma_1 = \Gamma_2$ is fixed at three and D is held constant, it follows from the previous section that the output voltage remains unchanged as the output power increases. Consequently, the current flowing through C_b increases with rising output power, which naturally leads to larger values of $V_{pk,1}$ and $V_{pk,2}$, corresponding to an increased voltage ripple. As $V_{pk,1}$ and $V_{pk,2}$ increase, maintaining (12) and (11) requires $\cos(\theta_1)$ and $\cos(\theta_2)$ to decrease, which in turn implies an increase in θ_1 and $|\theta_2|$. As the phase shifts become larger, the waveforms appear more linear. It is also illustrated in Fig. 8 that PLECS simulation waveforms exhibit strong alignment with theoretical calculation, thereby providing initial validation for the proposed model.

F. INDUCTOR CURRENT RIPPLE

Inductor current ripple plays a critical role in inductor value selection and, consequently, in determining the total inductor volume. Excessive inductor current ripple may also diminish the potential benefit of input current continuity for EMI filter size reduction. The top inductor current $i_{L_t}(t)$ is linear in phase one and sinusoidal in phase two, whereas the bottom inductor current $i_{L_b}(t)$ exhibits the opposite behavior. Accordingly, if the sinusoidal segment is monotonic over the phase interval, the ripple can be evaluated from the linear portion; otherwise, it must be determined from the extrema of the sinusoidal waveform. Therefore, assuming the inductor current as purely linear can underestimate the ripple whenever the sinusoidal segment is non-monotonic, potentially leading to undersized inductors. Fig. 9 illustrates how the inductor current varies with Γ_{min}. A larger Γ_{min} corresponds to a shorter phase interval, over which the extracted sinusoidal segment appears more linear.

G. COMPARISON BETWEEN THE LINEAR AND PROPOSED MODELS

With the proposed model established, the sources of inaccuracy in the linear model become evident. First, the linear model assumes a fixed output voltage, $V_{out} = DV_{in}$, whereas the actual output voltage depends on Γ_1 and Γ_2, as shown in (21). As Γ_{min} decreases, the deviation between the actual output voltage and DV_{in} increases. Since the capacitor voltage ripple and inductor current ripples are functions of the output

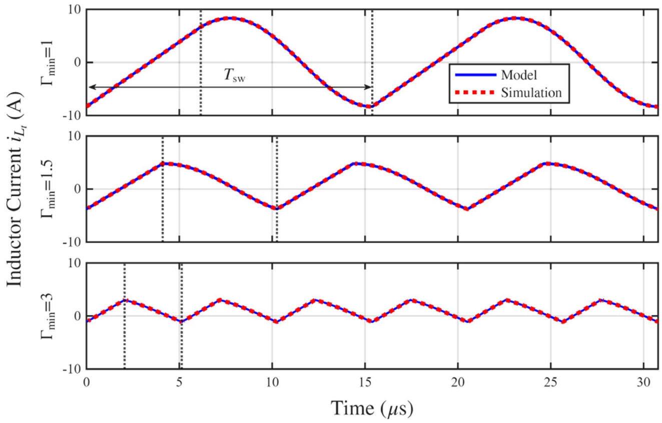

(a)

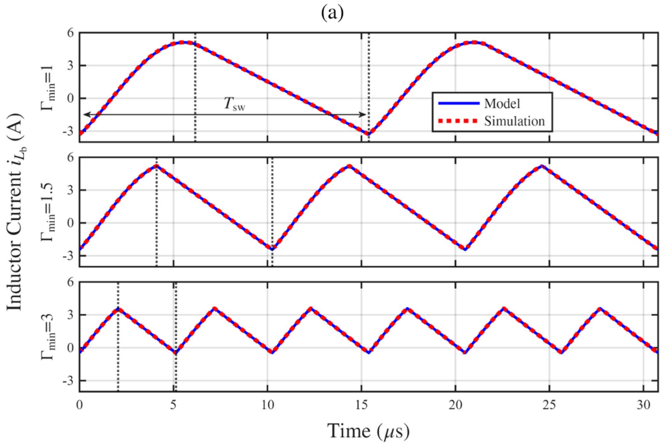

(b)

FIGURE 9. Calculated and simulated (a) inductor current i_{L_t} and (b) inductor current i_{L_b} waveforms under three different switching frequencies. $\Gamma_1 = \Gamma_2 = \Gamma_{min}$ because $L_t = L_b$. R_{load} = 15 Ω and other operating conditions are the same as in Fig. 8.

voltage, as indicated in (2) and (1), any discrepancy in V_{out} directly contributes to modeling error. This trend is reflected in Fig. 2. As Γ_{min} increases from $\Gamma_{min} = 1$ in Fig. 2(a) to $\Gamma_{min} = 5$ in Fig. 2(c), the inaccuracy in the capacitor voltage waveform correspondingly diminishes. Second, the linear model considers only the linear ripple component while neglecting the nonlinear contribution. Consequently, as the actual waveforms become more sinusoidal, the inaccuracy of the linear model increases. For clarity in this work, the following terminology is defined: the converter behavior captured by the linear model is referred to as "first order", whereas the effects of the resonant ripple components and output voltage deviation are referred to as "second order". For example, Fig. 10 illustrates how the capacitor voltage ripple can be separated into first-order and second-order components.

III. EXTENSION TO COUPLED INPUT INDUCTORS

In [1], [11] the potential to improve magnetic component utilization by coupling the two input inductors has been noted, but its effects on the current and voltage ripple in the input network and required passive volume have not been closely

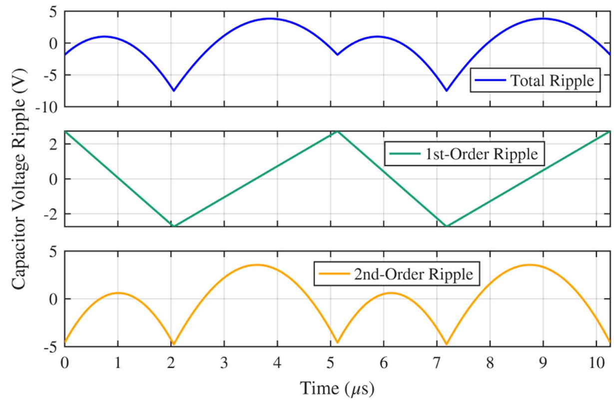

FIGURE 10. Decomposition of the capacitor voltage ripples into first-order and second-order ripple components. The passive component values and the operating condition are the same as Fig. 2(b) and Fig. 8(a).

analyzed. In addition, due to an equivalence between coupling the input inductors and output inductance, the following analysis of coupling in this section and Section IV can additionally be applied to compare CSBCs with conventional buck converters. A derivation of this equivalence and a comparison between the passive volume required in CSBCs and conventional buck converters is detailed in Appendix A and B.

After coupling the two input inductors, the schematic illustrated in Fig. 1 is generalized to the coupled case as shown in Fig. 11(a). The coupling of the top and bottom inductors is represented by leakage inductors $L_{\ell t}$, $L_{\ell b}$, an ideal transformer, and a magnetizing inductor L_μ [16], [17]. To simplify the analysis, it is assumed that the turns ratio of the transformer is 1:1. A non-unity turns ratio coupled inductor can be mapped to an equivalent 1:1 model, enabling the direct application of the equations in this work to an arbitrary coupled inductor [18]. However, the mapping process can produce negative inductances, potentially resulting in computation and simulation issues [19].

With a unity turns ratio, Kirchhoff's Current Law (KCL) gives the expression for the magnetizing inductor current,

$$i_{L_\mu}(t) = i_{L_{\ell t}}(t) + i_{L_{\ell b}}(t). \tag{23}$$

Using (23), the voltage across the magnetizing inductance can be expressed in terms of the current in each leakage inductor. The expression for $v_{L_\mu}(t)$ in (24) is applicable during either switching phase.

$$v_{L_\mu}(t) = L_\mu \frac{di_{L_\mu}}{dt} = L_\mu \left(\frac{di_{L_{\ell t}}(t)}{dt} + \frac{di_{L_{\ell b}}(t)}{dt} \right). \tag{24}$$

A. PHASE ONE

From Fig. 11(b), accounting for the phase one magnetizing inductance voltage $v_{L_\mu,1}(t)$ results in the following KVL equations:

$$v_{C_b,1}(t) = V_{out} + v_{L_\mu,1}(t) + v_{L_{\ell b},1}(t) \tag{25}$$

$$v_{L_{\ell t},1}(t) = V_{in} - v_{L_\mu,1}(t) - V_{out}. \tag{26}$$

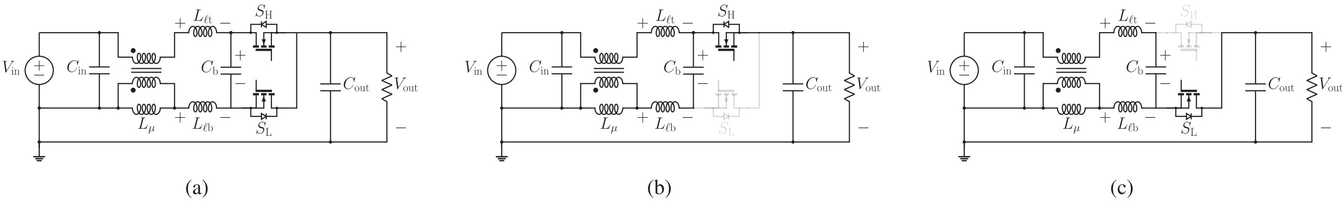

FIGURE 11. (a) Schematic of the C-CSBC, indicating (b) phase one operation and (c) phase two operation.

TABLE 3. Definition of Coupled Inductor Equation Constants

Parameter	Symbol	Value
Magnetizing-to-Self Inductance Ratio	γ_t	$\frac{L_\mu}{L_\mu+L_{\ell t}}$
Magnetizing-to-Self Inductance Ratio	γ_b	$\frac{L_\mu}{L_\mu+L_{\ell b}}$
Phase One Effective Resonant Inductance	L_{e1}	$L_{\ell b}+(L_{\ell t}\|L_\mu)$
Phase Two Effective Resonant Inductance	L_{e2}	$L_{\ell t}+(L_{\ell b}\|L_\mu)$

As in the uncoupled case during phase one, the current through the bottom inductor, $i_{L_{\ell b}}(t)$, flows only into C_b, which results in

$$v_{L_{\ell b},1}(t) = L_{\ell b}\frac{di_{L_{\ell b},1}(t)}{dt} = -L_{\ell b}\frac{di_{C_b,1}(t)}{dt} = -C_bL_{\ell b}\frac{d^2v_{C_b,1}(t)}{dt^2}. \quad (27)$$

Substituting (26) and (27) into (24) results in

$$v_{L_\mu,1}(t) = \frac{L_\mu}{L_\mu+L_{\ell t}}\left(V_{in}-V_{out}-L_{\ell t}C_b\frac{d^2v_{C_b,1}(t)}{dt^2}\right). \quad (28)$$

Combining (25), (27) and (28) produces a second-order linear ordinary differential equation defining the capacitor voltage behavior:

$$C_b(L_{\ell b}+L_\mu\|L_{\ell t})\frac{d^2v_{C_b,1}(t)}{dt^2} = V_{out}+\frac{L_\mu}{L_\mu+L_{\ell t}}(V_{in}-V_{out})-v_{C_b,1}(t). \quad (29)$$

To simplify the equations, a set of four constants are introduced in Table 3. In terms of the effective resonant inductance, the phase one resonant frequency can be written as $\omega_1 = 1/\sqrt{L_{e1}C_b}$. Using the phase-shifted cosine representation from (8), the bypass capacitor voltage can be written as

$$v_{C_b,1}(t) = V_{pk,1}\cos(\omega_1 t+\theta_1)+V_{out}+\gamma_t(V_{in}-V_{out}). \quad (30)$$

Notably, the capacitor voltage waveform has a similar form to (8), with an altered resonant frequency and modified constant term dependent on γ_t, the magnetizing-to-self inductance ratio. Both values are constants that can be directly calculated from the leakage and magnetizing inductances.

B. PHASE TWO

Similarly, in phase two, the KVL equations accounting for the voltage across the magnetizing inductance are

$$\begin{aligned} v_{L_\mu,2}(t)+v_{L_{\ell t},2}(t) &= V_{in}-V_{out}-v_{C_b,2}(t)\\ v_{L_\mu,2}(t)+v_{L_{\ell b},2}(t) &= -V_{out}. \end{aligned} \quad (31)$$

The current in the top leakage inductor now only flows into the bypass capacitor, so the same approach can be taken as in phase one. In phase two, the resonant frequency is given by $\omega_2 = 1/\sqrt{L_{e2}C_b}$. The resulting equation for $v_{C_b,2}(t)$ is

$$v_{C_b,2}(t) = V_{pk,2}\cos(\omega_2 t+\theta_2)+V_{in}-V_{out}+\gamma_bV_{out}. \quad (32)$$

In phase two, the bypass capacitor voltage expression has a similar form to (10) with a modified constant term γ_bV_{out}. With the bypass capacitor voltage in each phase defined by (30) and (32), the voltage and current in all of the input passive components can be derived. These expressions are provided in Table 4.

C. DERIVATION OF SYSTEM EQUATIONS WITH COUPLING

To solve for the five unknowns ($V_{pk,1}$, $V_{pk,2}$, θ_1, θ_2, and V_{out}), the equations utilized in the uncoupled case, (11)–(15), must be modified to account for the effects of coupling. In particular, the voltages across the top and bottom leakage inductors are no longer linear in any phase due to the voltage across the magnetizing inductor, $v_{L_\mu}(t)$. The resulting volt-second balance equations for $L_{\ell t}$ and $L_{\ell b}$ respectively are

$$\frac{2V_{pk,2}}{\omega_2}\sin\left(\omega_2\frac{t_2}{2}\right)\cos(\theta_2) = (V_{in}-V_{out})t_1 - \gamma_bV_{out}t_2 \quad (33)$$

$$\frac{2V_{pk,1}}{\omega_1}\sin\left(\omega_1\frac{t_1}{2}\right)\cos(\theta_1) = V_{out}t_2 - \gamma_t(V_{in}-V_{out})t_1. \quad (34)$$

TABLE 4. Derived Expressions for Voltages and Currents in C-CSBCs

	Phase One $[-\frac{t_1}{2}, \frac{t_1}{2}]$	Phase Two $[-\frac{t_2}{2}, \frac{t_2}{2}]$
$v_{L_\mu}(t)$	$\gamma_t\left(V_{in} - V_{out} + \frac{L_{\ell t}V_{pk,1}}{L_{e1}}\cos(\omega_1 t + \theta_1)\right)$	$-\gamma_b\left(V_{out} + \frac{L_{\ell b}}{L_{e2}}V_{pk,2}\cos(\omega_2 t + \theta_2)\right)$
$v_{L_{\ell t}}(t)$	$(1-\gamma_t)(V_{in} - V_{out}) - \frac{\gamma_t L_{\ell t}V_{pk,1}}{L_{e1}}\cos(\omega_1 t + \theta_1)$	$-\frac{L_{\ell t}}{L_{e2}}V_{pk,2}\cos(\omega_2 t + \theta_2)$
$v_{L_{\ell b}}(t)$	$\left(1 - \frac{\gamma_t L_{\ell t}}{L_{e1}}\right)V_{pk,1}\cos(\omega_1 t + \theta_1)$	$\frac{\gamma_b L_{\ell b}}{L_{e2}}V_{pk,2}\cos(\omega_2 t + \theta_2) - (1-\gamma_b)V_{out}$
$v_{C_b}(t)$	$V_{pk,1}\cos(\omega_1 t + \theta_1) + V_{out} + \gamma_t(V_{in} - V_{out})$	$V_{pk,2}\cos(\omega_2 t + \theta_2) + V_{in} - (1-\gamma_b)V_{out}$
$i_{C_b}(t)$	$-V_{pk,1}C_b\omega_1\sin(\omega_1 t + \theta_1)$	$-V_{pk,2}C_b\omega_2\sin(\omega_2 t + \theta_2)$
$i_{L_\mu}(t)$	$i_{L_{\ell t},1}(t) + i_{L_{\ell b},1}(t)$	$i_{L_{\ell t},2}(t) + i_{L_{\ell b},2}(t)$
$i_{L_{\ell t}}(t)$	$i_{L_{\ell t},2}\left(\frac{t_2}{2}\right) + \frac{(1-\gamma_t)(V_{in}-V_{out})}{L_{\ell t}}(t + \frac{t_1}{2})$ $-\frac{\gamma_t V_{pk,1}}{L_{e1}\omega_1}\left(\sin(\omega_1 t + \theta_1) + \sin(\omega_1\frac{t_1}{2} - \theta_1)\right)$	$-V_{pk,2}C_b\omega_2\sin(\omega_2 t + \theta_2)$
$i_{L_{\ell b}}(t)$	$V_{pk,1}C_b\omega_1\sin(\omega_1 t + \theta_1)$	$i_{L_b,1}\left(\frac{t_1}{2}\right) - \frac{(1-\gamma_b)V_{out}}{L_{\ell b}}\left(t + \frac{t_2}{2}\right)$ $+\frac{\gamma_b V_{pk,2}}{L_{e2}\omega_2}\left(\sin(\omega_2 t + \theta_2) + \sin(\omega_2\frac{t_2}{2} - \theta_2)\right)$

The voltage continuity equations of $v_{C_b}(t)$ between the two phases are similar to the uncoupled case, except for the addition of the modified constant terms as described in (30) and (32). The resulting equations are

$$V_{pk,1}\cos\left(\omega_1\frac{t_1}{2} + \theta_1\right) + V_{out} + \gamma_t(V_{in} - V_{out}) = V_{pk,2}\cos\left(\omega_2\frac{-t_2}{2} + \theta_2\right) + V_{in} - V_{out} + \gamma_b V_{out} \tag{35}$$

$$V_{pk,1}\cos\left(\omega_1\frac{-t_1}{2} + \theta_1\right) + V_{out} + \gamma_t(V_{in} - V_{out}) = V_{pk,2}\cos\left(\omega_2\frac{t_2}{2} + \theta_2\right) + V_{in} - V_{out} + \gamma_b V_{out}. \tag{36}$$

Equation (15) is used to provide the last required equation, which enforces that the sum of the average current output from the leakage inductors is equal to the average output current. Applying the expressions for $v_{L_\mu}(t)$ from Table 4 results in the following expressions for I_1 and I_2:

$$\begin{aligned} I_1 = {} & \frac{V_{in} - V_{out}}{2(L_\mu + L_{\ell t})}t_1^2 - V_{pk,2}C_b\omega_2 t_1\sin\left(\omega_2\frac{t_2}{2} + \theta_2\right) \\ & + 2(1-\gamma_t)V_{pk,1}C_b\sin\left(\omega_1\frac{t_1}{2}\right)\sin(\theta_1) \\ & - \gamma_t C_b V_{pk,1}\omega_1 t_1\sin\left(\omega_1\frac{t_1}{2} - \theta_1\right) \end{aligned} \tag{37}$$

$$\begin{aligned} I_2 = {} & \frac{-V_{out}}{2(L_\mu + L_{\ell b})}t_2^2 + V_{pk,1}C_b\omega_1 t_2\sin\left(\omega_1\frac{t_1}{2} + \theta_1\right) \\ & - 2(1-\gamma_b)V_{pk,2}C_b\sin\left(\omega_2\frac{t_2}{2}\right)\sin(\theta_2) \\ & + \gamma_b V_{pk,2}C_b\omega_2 t_2\sin\left(\omega_2\frac{t_2}{2} - \theta_2\right). \end{aligned} \tag{38}$$

In summary, coupling the input inductors augments the five equations required to solve for $V_{pk,1}$, $V_{pk,2}$, θ_1, θ_2, and V_{out}. These equations are given by (33)–(36), and (15) with the coupled expressions for I_1 and I_2 given by (37) and (38). The effect of coupling appears as changes in the resonant frequency of each phase, and additional terms dependent on γ_t and γ_b. If there is no coupling, $L_\mu = 0$ and $L_{\ell t}$, $L_{\ell b}$ are treated as the two uncoupled input inductors, in which case (33)–(38) reduce to (11)–(17).

The strength of coupling in a coupled inductor is often expressed using the coupling coefficient k. For the unity turns ratio case considered here, the coupling coefficient is given by

$$k = \frac{L_\mu}{\sqrt{L_{self1}L_{self2}}}, \tag{39}$$

with $L_{self1} = L_\mu + L_{\ell t}$ and $L_{self2} = L_\mu + L_{\ell b}$. The coupling coefficient can alternatively be expressed in terms of the magnetizing-to-self inductance ratios defined in Table 3.

$$k = \sqrt{\gamma_t\gamma_b} \tag{40}$$

Thus, γ_t and γ_b are closely associated with the coupling coefficient of the coupled inductor. If the coupled inductor is implemented using symmetrical magnetic structure such that $L_{\ell t} = L_{\ell b}$, the coupling coefficient and magnetizing-to-self inductance ratios are all equal, i.e. $k = \gamma_t = \gamma_b$.

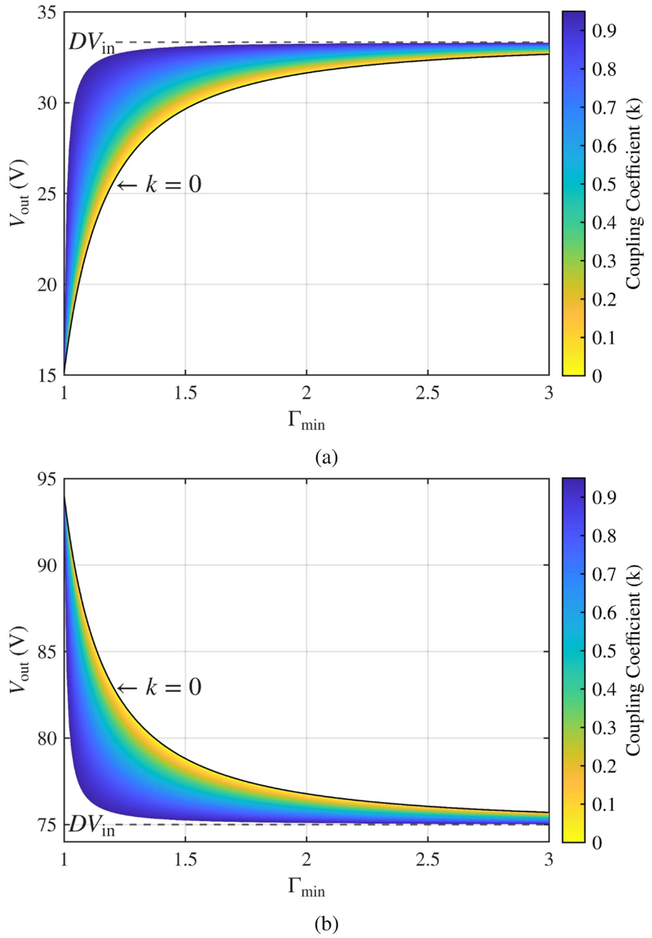

FIGURE 12. Modeled effect of coupling on output voltage as a function of Γ_{min} with a symmetrical coupled inductor for $V_{in} = 100$ V. The symmetrical coupled inductor produces $\gamma_t = \gamma_b = k$ and $\Gamma_1 = \Gamma_2 = \Gamma_{min}$. The duty cycles are (a) $D = 1/3$ and (b) $D = 3/4$.

D. OUTPUT VOLTAGE

In the coupled case, the analytical expression for the output voltage is obtained by combining (33)–(36).

$$V_{out} = V_{in} \times \frac{2\pi D\left[\dfrac{\frac{\gamma_t}{\Gamma_1}}{\tan\left(\frac{\pi D}{\Gamma_1}\right)} + \dfrac{\frac{1}{\Gamma_2}}{\tan\left(\frac{\pi(1-D)}{\Gamma_2}\right)}\right] + 2(1-\gamma_t)}{2\pi\left[\dfrac{\frac{1-D(1-\gamma_t)}{\Gamma_1}}{\tan\left(\frac{\pi D}{\Gamma_1}\right)} + \dfrac{\frac{D+\gamma_b(1-D)}{\Gamma_2}}{\tan\left(\frac{\pi(1-D)}{\Gamma_2}\right)}\right] + 4 - 2(\gamma_t+\gamma_b)}, \quad (41)$$

where Γ_1 and Γ_2 are the previously defined parameters from (19)–(20), and the duty ratio is given in (9). As in the uncoupled case, if $D = 1/2$ and $\Gamma_1 = \Gamma_2$, the output voltage is given by the nominal conversion ratio $V_{out} = DV_{in}$ regardless of the resonant frequencies or coupling coefficient.

Fig. 12 showcases the effect of coupling on the voltage conversion ratio for $D \in \{1/3, 3/4\}$ as Γ_{min} is increased for a symmetrical coupled inductor. The output voltage at resonance is unaffected by coupling, but convergence to its nominal value occurs at lower values of Γ_{min} with stronger coupling. This result aligns with the limit of the output voltage equation as the coupling coefficient approaches one,

$$\lim_{k\to 1} V_{out} = DV_{in}, \quad (42)$$

indicating that the output voltage has no switching frequency dependence for a fully coupled inductor.

IV. EFFECT OF COUPLING ON PASSIVE VOLUME

As the nonlinear system of equations derived in Sections II and III lack analytical solutions, the effects of coupling on component volume are not immediately clear. As a result, understanding the impact of coupling on passive component volume and practical differences between U-CSBCs and C-CSBCs requires an in-depth analysis.

The remainder of this section is structured into analysis of several primary considerations regarding coupling in CSBCs. Section IV-A describes how coupling affects bypass capacitor sizing. Section IV-B derives a calculation for the best case reduction in magnetic component volume achievable by coupling in a ripple-limited design. Section IV-C presents an overview of important practical considerations regarding coupling. Section IV-D concludes this section with a summary of the key design insights for coupling in C-CSBCs.

A. EFFECT OF COUPLING ON BYPASS CAPACITOR AND RESONANT FREQUENCIES

As coupling alters the effective resonant inductances of the converter, it significantly affects the sizing of the bypass capacitor C_b. This is most clear when k approaches one, as the magnetizing inductance becomes much larger than the leakage inductances, and the effective resonant inductances from Table 3 are approximately $L_{e1} \approx L_{e2} \approx (L_{\ell t} + L_{\ell b})$. Thus, as leakage inductance is decreased in a tightly coupled inductor, the effective resonant inductances decrease as well, aligning with the results from [1], where coupling is observed to worsen small signal converter stability.

For a given switching frequency, the bypass capacitance must be increased to counteract the effects of the decreased effective resonant inductances to ensure the resonant frequencies remain sufficiently below the switching frequency. However, to evaluate this increase in required bypass capacitance between due to coupling, the input current ripples must be constrained to provide a fair comparison. To constrain the first-order ripples, the linear model can be utilized to express the inductances as a function of the ripple constraints, $\Delta i_{t,max}$ and $\Delta i_{b,max}$. The equations are parametrized using the parallel leakage inductance $L_x = L_{\ell t} \| L_{\ell b}$.

$$L_\mu = \frac{V_{in} T_{sw}(D_\Delta - D_\Delta^2)}{\Delta i_{t,max} + \Delta i_{b,max}} - L_x \quad (43)$$

$$L_{\ell t} = L_x\left(1 + \frac{\Delta i_{b,max}}{\Delta i_{t,max}}\right) \quad (44)$$

$$L_{\ell b} = L_x \left(1 + \frac{\Delta i_{t,max}}{\Delta i_{b,max}}\right), \tag{45}$$

Combining (44) and (45) results in

$$\frac{L_{\ell b}}{L_{\ell t}} = \frac{\Delta i_{t,max}}{\Delta i_{b,max}}, \tag{46}$$

indicating that the ratio between the two input ripple constraints is equivalent to the reciprocal ratio of the corresponding inductors. Note that the inductors must be designed based on the duty cycle where the maximum current ripple occurs, which is denoted as D_Δ and is the same for all inductors in the linear model.

To constrain the second-order input current ripples, Γ_{min} is kept fixed. In other words, Γ_{min} is treated as an analytical constraint on the second-order converter behavior. With the first- and second-order components of the CSBC input current ripples constrained, the increase in required bypass capacitance due to coupling can be fairly calculated. This increase is $C_{b,c}/C_{b,u}$ where 'c' and 'u' denote the coupled and uncoupled designs respectively. The value of $C_{b,c}/C_{b,u}$ required to maintain the same Γ_{min} can be expressed as a function of the coupling coefficient k and an additional parameter $L_R = \max\{\frac{L_{\ell t}}{L_{\ell b}}, \frac{L_{\ell b}}{L_{\ell t}}\}$. The expression for $C_{b,c}/C_{b,u}$ is derived by combining (1), (40), (43), (46) and the resonant frequencies calculations. The derived expression is generally complex, but has straightforward bounds. The lower bound occurs when $L_R \to \infty$ and the upper bound occurs when $L_R = 1$.

$$\left.\frac{C_{b,c}}{C_{b,u}}\right|_{\text{lower bound}} = \frac{1}{1-k^2} \tag{47}$$

$$\left.\frac{C_{b,c}}{C_{b,u}}\right|_{\text{upper bound}} = \frac{1}{1-k} \tag{48}$$

The behavior of $C_{b,c}/C_{b,u}$ is plotted as a function of k for the range of L_R in Fig. 13. Equivalently, if the bypass capacitor is kept fixed, the value of Γ_{min} for the U-CSBC is $\sqrt{C_{b,u}/C_{b,c}}$ times greater than the value of Γ_{min} for the C-CSBC, which is shown in Fig. 13 as well. It can be concluded that at a given switching frequency, the required bypass capacitor to maintain Γ_{min} increases monotonically with k for any inductor current ripple constraints, and is unbounded as k approaches one. If the bypass capacitance is not increased, the converter's Γ_{min} will decrease, resulting in larger second-order ripples and eventual constraint violation.

B. EFFECT OF COUPLING ON MAGNETIC COMPONENT ENERGY STORAGE REQUIREMENTS

From the preceding analysis, it can be concluded that coupling has detrimental effects on the second-order converter behavior due to the decrease in effective resonant inductances. To compensate, the bypass capacitance, switching frequency, or ripple constraints must be increased. In practice, these deleterious second-order effects limit coupling strength, but may be warranted if coupling is able to reduce magnetic component volume. Therefore, an analysis of magnetic component volume which neglects the second-order effects of coupling is warranted. This can be accomplished using the linear model equations (43)–(45). A visualization of the effects of coupling on the inductor current ripple when using the linear equations to size the inductances is provided in Fig 14. As the coupling is increased, the second-order ripple is increased, but the first-order ripple remains unaffected. Effectively, analysis based on the linear C-CSBC model presents the "best case" for coupling, enabling the coupling strength to be set arbitrarily, and facilitating analysis of the fundamental potential for coupling to reduce magnetic component volume. If coupling is deemed to be effective for a particular design, the model developed in Section III can be applied to optimize the tradeoff between coupling strength and increased bypass capacitance.

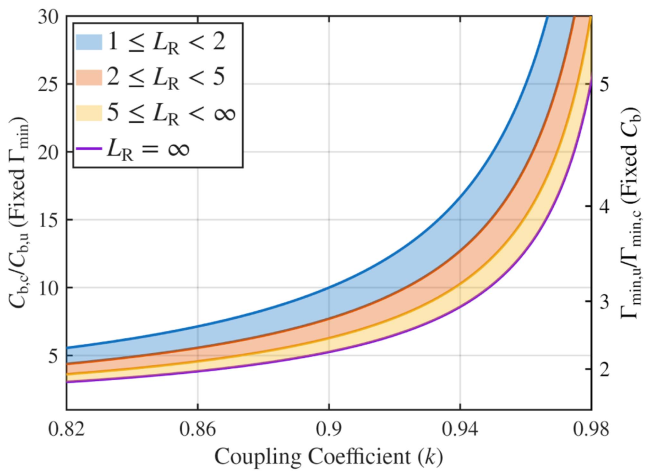

FIGURE 13. Left axis: required increase in C-CSBC bypass capacitance as a function of k for a fixed Γ_{min}. Right axis: increase in U-CSBC Γ_{min} as a function of k for a fixed bypass capacitance. The shaded areas correspond to different ranges of L_R.

To calculate the potential reduction in magnetic component volume, it is assumed that all inductors have the same, fixed energy density $\rho_{E,L}$. As a result, the total magnetic component volume is proportional to the sum of each magnetic component's maximum energy storage requirement, denoted as E_{mag}.

$$\text{Vol}_{mag} \propto E_{mag} = \frac{1}{2}(L_{\ell t} i^2_{L_{\ell t},pk} + L_{\ell b} i^2_{L_{\ell b},pk} + L_\mu i^2_{L_\mu,pk}) \tag{49}$$

The maximum achievable reduction in magnetic component volume by coupling is parameterized as the best-case reduction in total required magnetic energy storage φ_c.

$$\varphi_c = \left.\frac{\text{Min. Coupled } E_{mag}}{\text{Min. Uncoupled } E_{mag}}\right|_{\text{linear model}} \tag{50}$$

Due to the assumed constant energy density, the reduction in total maximum magnetic energy storage is equivalent to reduction in magnetic component volume. Note that in general, the maximum energy storage requirement for each component can occur at different points. Therefore, each component's peak energy storage requirement must be found individually and summed to determine E_{mag}. The expression for the

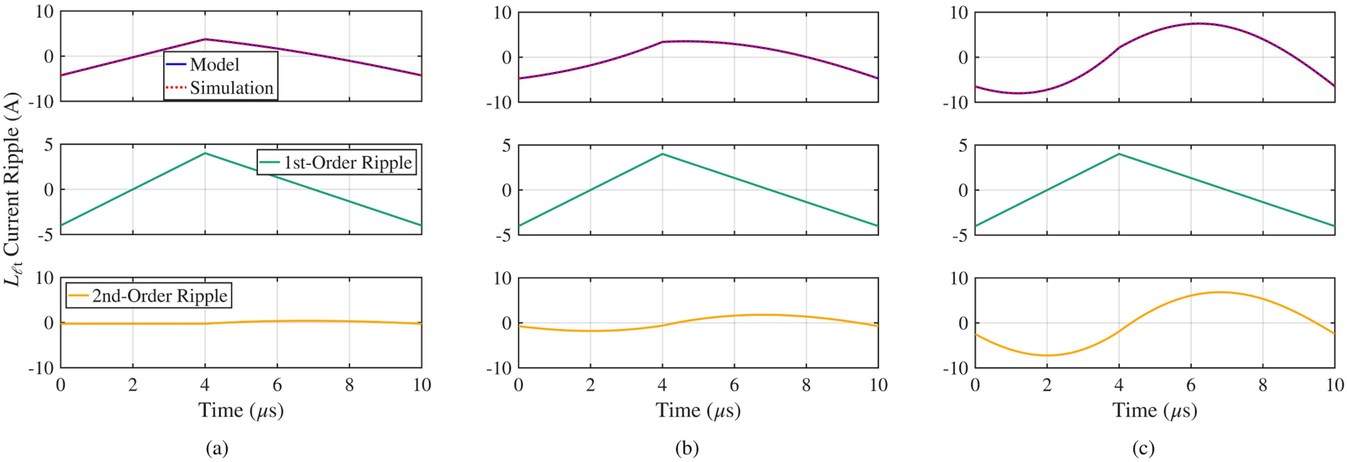

FIGURE 14. **Modeled increase in second-order input current ripple due to coupling. The converter design specifications are $V_{in} = 100$ V, $R_{load} = 1.5\ \Omega$, $D = 0.4$, $f_{sw} = 100$ kHz, $C_b = 250$ nF, and $\Delta i_{t,max} = \Delta i_{b,max} = 8$ A. The magnetic components are sized utilizing the linear model equations in (43)–(45), which results in identical first-order ripples regardless of k. However, as the coupling strength is increased without changing C_b, the resonant frequencies are increased resulting in larger second-order ripple components and significant inductor current ripple constraint violation. The coupling coefficients are (a) $k = 0$, (b) $k = 0.5$, and (c) $k = 0.8$.**

best-case reduction in magnetic energy storage from coupling parameter φ_c depends on the particular set of design constraints. To provide an example for the calculation of φ_c, and how its value can be applied to determine the situations in which coupling is effective in reducing component volume, the case of a ripple-limited design is considered. In a ripple-limited design, the magnetic component volume is minimized by using the smallest inductances which satisfy the constraints, given in (43)–(45). The ripple constraints, $\Delta i_{t,max}$ and $\Delta i_{b,max}$ are assumed to be constant between coupled and uncoupled implementations to enable direct comparison.

To minimize E_{mag}, the optimal value of the parallel leakage inductance L_x must be found. Substituting (43)–(45) into (49), the derivative of the magnetic energy storage with respect to L_x is

$$\frac{\partial E_{mag}}{\partial L_x} = \frac{1}{2}\left[\left(1 + \frac{\Delta i_{b,max}}{\Delta i_{t,max}}\right) i^2_{L_{\ell t},pk} + \left(1 + \frac{\Delta i_{t,max}}{\Delta i_{b,max}}\right) i^2_{L_{\ell b},pk} - i^2_{L_\mu,pk}\right]. \tag{51}$$

As (51) is a constant, its sign indicates if increasing L_x increases or decreases magnetic energy storage. If (51) is zero, this means that the same total energy storage is required for any value of L_x. Given that $i_{L_\mu}(t) = i_{L_{\ell t}}(t) + i_{L_{\ell b}}(t)$, it follows that $i_{L_\mu,pk} \leq (i_{L_{\ell t},pk} + i_{L_{\ell b},pk})$. Noting that $i^2_{L_\mu,pk}$ is the only subtracted term in (51), and all other terms are positive, setting $i_{L_\mu,pk} = (i_{L_{\ell t},pk} + i_{L_{\ell b},pk})$ produces its minimum value:

$$\min\left(\frac{\partial E_{mag}}{\partial L_x}\right) = \frac{1}{2}\left(\sqrt{\frac{\Delta i_{b,max}}{\Delta i_{t,max}}}\, i_{L_{\ell t},pk} - \sqrt{\frac{\Delta i_{t,max}}{\Delta i_{b,max}}}\, i_{L_{\ell b},pk}\right)^2. \tag{52}$$

As the minimum derivative of the magnetic component volume with respect to L_x can be expressed as a positive multiple of a real number squared, it is always greater than or equal to zero. Consequently, increasing L_x can never decrease magnetic energy storage. As L_x is the parallel leakage inductance, its minimum value is zero, so the minimum magnetic energy storage requirements are always achieved with $L_x = 0$. From (44) and (45), this means that magnetic component volume is minimized by using $L_{\ell t} = L_{\ell b} = 0$. The volume for an uncoupled design can be determined by setting $L_\mu = 0$, so φ_c can be expressed as

$$\varphi_c = \frac{L_\mu i^2_{L_\mu,pk}\Big|_{L_x=0}}{\left(L_{\ell t} i^2_{L_{\ell t},pk} + L_{\ell b} i^2_{L_{\ell b},pk}\right)\Big|_{L_\mu=0}} = \frac{i^2_{L_\mu,pk}}{\left(1 + \frac{\Delta i_{b,max}}{\Delta i_{t,max}}\right) i^2_{L_{\ell t},pk} + \left(1 + \frac{\Delta i_{t,max}}{\Delta i_{b,max}}\right) i^2_{L_{\ell b},pk}}. \tag{53}$$

Assuming a constant $\rho_{E,L}$, U-CSBC inductor volume is minimized by using the same ripple ratio (the ratio of the peak-to-peak ripple to the maximum dc current, $\Delta i_{n,max}/I_n$) for each input inductor. In this case, (53) can be simplified as

$$\varphi_c\big|_{\text{matching ripple ratios}} = \left(\frac{i_{L_\mu,pk}}{i_{L_{\ell t},pk} + i_{L_{\ell b},pk}}\right)^2. \tag{54}$$

Equation (53) can be applied for any design where the input current ripple constraints are constants, and the coupled inductor is implemented using a unity turns ratio, while (54) can be applied for any design meeting these conditions and having the same current ripple ratio for both input branches.

A common practice is to set the inductor current ripple ratio to 20–40% to limit ac losses and EMI [20], [21]. With a constant input voltage and current ripple ratio, φ_c is a function of the duty cycle range, set by $D \in [D_{min}, D_{max}]$, and the

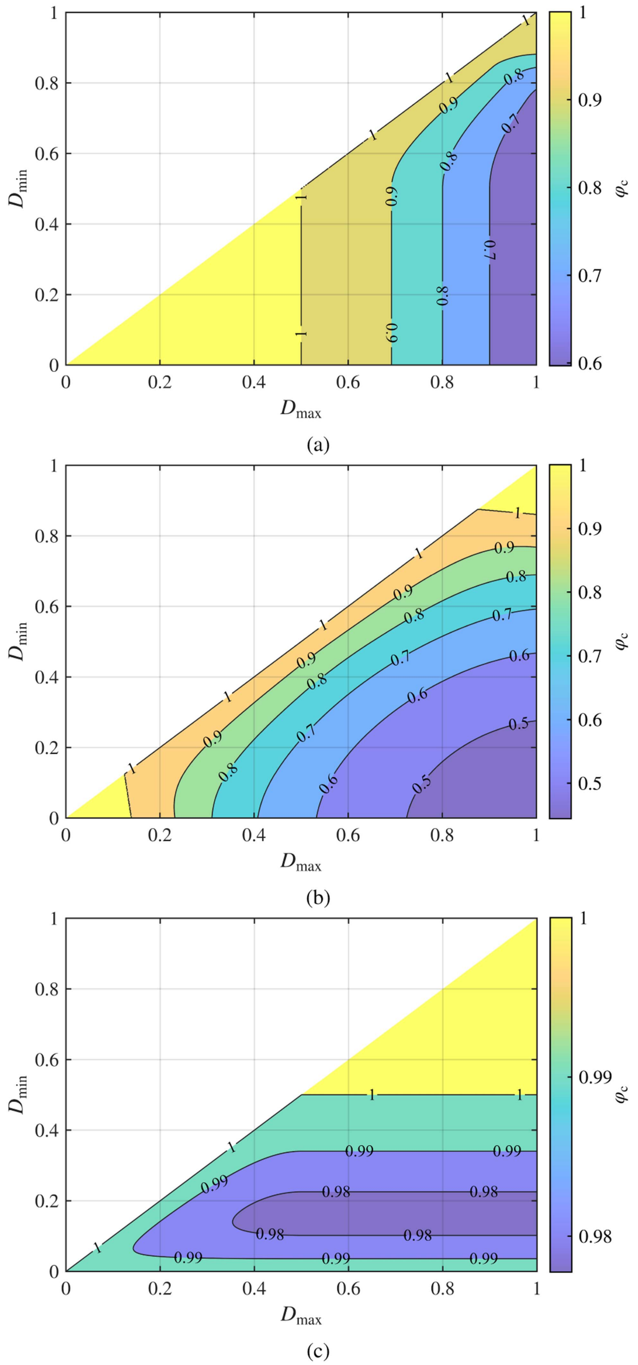

FIGURE 15. Values of φ_c for fixed input voltage (a) CR, (b) CC, and (c) CP loads. The branch peak-to-peak ripple constraints are 1/3 of the maximum dc branch current.

load type, which is application dependent. Constant resistance (CR), constant current (CC), or constant power (CP) loads are widely used for modeling purposes [22]. Fig. 15 shows contour plots of φ_c for CR, CC, or CP loads, where $\Delta i_{t,max}$ and $\Delta i_{b,max}$ are set to 1/3 of the maximum dc current in their respective branches. In CR and CC loads, values of φ_c substantially below one are observed for wide duty cycle ranges, with CC loads providing the smallest values overall. Conversely, $\varphi_c = 1$ if $D_{min} = D_{max}$, regardless of load type, and for CP loads, the minimum value of φ_c is $0.9\bar{7}$. In summary, wide-range converter operating conditions, such as a wide duty cycle range specification, are required for coupling to reduce total magnetic component energy storage requirements, but the behavior of φ_c varies significantly depending on the load type.

C. PRACTICAL DESIGN CONSIDERATIONS FOR COUPLED INDUCTORS

From a theoretical perspective, coupling results in a fundamental tradeoff between the potential to reduce magnetic component volume, at the cost of requiring a larger bypass capacitance to offset the reduced effective resonant inductances. However, in choosing between a coupled or uncoupled CSBC implementation, designers must also weigh the practical implications of coupling. Firstly, it is important to consider the limitations of the energy storage based analysis used to calculate component volume. In practice, the scaling laws of magnetic components suggest that a single, larger inductor has higher energy density than multiple smaller inductors [12], which is beneficial for coupling. Also, the actual inductor volume is primarily determined by core selection, which may favor coupled or uncoupled designs, depending on component availability. Therefore, the true effect on magnetic component volume due to coupling generally will differ from the theoretical effect determined by φ_c.

Another important consideration for use of coupled magnetics is the substantial increase in magnetic component design complexity. A particularly difficult task is the precise and reliable design of the leakage inductances, which depend strongly on many parameters including inductor geometry [23], [24], [25]. Depending on the application, a wide range of approaches have been described in literature, including custom core structures [17], magnetic shunts [26], and multi-phase windings [27]. The multi-phase approach requires more than two windings, making it inapplicable to the single-phase CSBC. Meanwhile, the design of unique core structures adds complexity and cost, and typical leakage inductance errors generally remain higher than for uncoupled inductor design [28], [29]. In tightly coupled designs, the energy storage requirements of the leakage inductances are minimal. Despite this, as reflected in (44)–(45), the *relative* leakage inductance values significantly affect the input branch current ripples, meaning the particular value of the leakage inductances noticeably affects converter performance, even in tightly coupled cases.

The dependence of the input branch ripples on the leakage inductances has historically been a topic of interest in various topologies utilizing coupled inductors, with significant research effort devoted to "ripple steering", or "zero ripple" techniques. The concept was initially applied to and is strongly associated with the Ćuk converter [30], [31], but the mechanism has been applied generally [32], [33], [34]. Notably, the potential application of ripple steering to the CSBC has been specifically described in [33], [35], though not analyzed in detail. The ripple steering mechanism can be explained by the use of a decoupled model (an equivalent circuit using only uncoupled inductors). In the case of the C-CSBC, the use of a 1:1 coupled inductor is electrically equivalent to placing L_μ at the output as in a conventional buck converter, while the leakage inductances appear at the input. This decoupled model is derived and analyzed in Appendix A and B.

The ripple steering technique enables the elimination of first-order input current ripple without additional magnetic components, but requires precise leakage inductor design. Symmetrical coupled inductors provide a good compromise between performance and magnetic design complexity by reducing the sensitivity of the coupled inductor to factors such as manufacturing variation [36], [37], [38]. Using symmetrical leakage inductances is not optimal for passive volume minimization in all cases, but the leakage inductance volume can be reduced with a high coupling coefficient. Depending on the converter operating point, the resulting input current ripple for the symmetrical C-CSBC may be increased or decreased compared to a U-CSBC. In general, methods for designing the coupled inductor in a CSBC trade off performance for simplicity, and the most effective implementation depends on design specifications and the motivation for coupling.

Though the analysis conducted here focuses on passive component volume, inductor loss is an additional important design consideration which is influenced by coupling. Comparing loss between uncoupled or coupled designs is difficult in general. Assuming a constant quality factor, the preceding analysis of coupling on volume applies to loss minimization as well. However, it is unlikely that the quality factors of an uncoupled and coupled inductor would be the same, as the various winding strategies for coupled inductors significantly affect dc and ac winding loss [39], [40], [41]. The effect of coupling on core loss is also challenging to quantify in general. The potential decrease in magnetic component volume via coupling occurs largely due to improved core utilization, which corresponds to increased peak-to-peak flux swing in the core, increasing core loss density. In addition, the dc magnetic field in the core is impacted by coupling, an effect which is not well represented even by improved variants of Steinmetz Equation, though various studies have demonstrated core loss increase with larger dc bias [42], [43], [44]. At the same time, the potential decrease in core volume from coupling can reduce core loss. Overall, the impact of coupling on inductor losses varies nonlinearly with many design parameters, and is best evaluated on a case-to-case basis.

D. SUMMARY OF COUPLED INDUCTOR DESIGN CONSIDERATIONS

The preceding analysis of coupling reveals the following design insights relevant for C-CSBCs:

- For given inductor current ripple constraints, tighter coupling results in decreased effective resonant inductances in the input passive network. This effect can be compensated for by increasing the bypass capacitance.
- In wide-range converters, coupling can directly reduce the total maximum magnetic energy storage requirements in a CSBC. The achievable reduction can be calculated using (53) for arbitrary input current ripple constraints, or (54) assuming matching input ripple ratios.
- The leakage inductances of a C-CSBC significantly affect input ripple and present challenge in the magnetic domain. At the same time, the leakage inductance volume can be reduced by increased coupling, making their design more flexible than the inductors of a U-CSBC.

V. COMPONENT SELECTION AND DESIGN EXAMPLE

This section provides a design example to illustrate how the proposed model can be utilized to optimally size the passive components in a C-CSBC. For comparison, a brief overview of the conventional component sizing approach using the linear model is presented first.

A. LINEAR COMPONENT SELECTION

In prior work [1], [3], [5], [7], [10], [11], [15], the input network passive components are selected by applying linear ripple calculations to size the inductors. The bypass capacitor must then be selected conservatively to reduce the resonant frequencies far below the switching frequency. This approach is generally reasonable because the inductor volume is typically much greater than the bypass capacitor volume, and the linear model provides the minimum inductances required to meet the ripple constraints. To size the bypass capacitor, the designer must select a sufficiently high value of $\Gamma_{\min}$ such that the second-order inductor current ripple is negligible. The required bypass capacitance is then

$$C_{\mathrm{b}} = \frac{\Gamma_{\min}^2}{4\pi^2 f_{\mathrm{sw}}^2 \min\{L_{\mathrm{e}1}, L_{\mathrm{e}2}\}}. \tag{55}$$

The designer must then verify that the chosen capacitance has acceptable voltage ripple using (2), and increase the capacitance if necessary. This approach is referred to as "Linear Component Selection" in this work.

1) LINEAR COUPLED COMPONENT SELECTION

While the linear approach is straightforward for U-CSBCs, the process requires special consideration for application to C-CSBCs. Due to the fundamental tradeoffs between coupling strength and required bypass capacitance analyzed in Section IV, selecting the proper coupling strength is important to minimize overall component volume in C-CSBCs. While this is generally analytically challenging, several approximations can be applied for tightly coupled C-CSBCs to arrive at closed form expressions for the optimal component values. In tightly coupled designs, the effective resonant inductances are approximately $L_{\mathrm{e}1} \approx L_{\mathrm{e}2} \approx (L_{\ell\mathrm{t}} + L_{\ell\mathrm{b}})$, as discussed in Section III. In addition, the peak bypass capacitor voltage is assumed to be constant and equal to V_{in}. This approximation is reasonable because the requirement to significantly increase the bypass capacitance in tightly coupled designs typically results in small capacitor ripple voltage. By applying the tight coupling approximation, (46), and (55), all component volumes are expressed as a function of $L_{\ell t}$. The resultant value of $L_{\ell t}$ which minimizes overall component volume is denoted as $L^*_{\ell t}$.

$$L^*_{\ell t} = \frac{\Gamma_{\min} V_{\text{in}}}{2\pi f_{\text{sw}}} \sqrt{\frac{\rho_{\text{E,L}}}{\rho_{\text{E,C}}\left(1 + \frac{\Delta i_{\text{t,max}}}{\Delta i_{\text{b,max}}}\right)}} \times \sqrt{\frac{1}{i^2_{L_{\ell t},\text{pk}} + \frac{\Delta i_{\text{t,max}}}{\Delta i_{\text{b,max}}} i^2_{L_{\ell b},\text{pk}} - \frac{\Delta i_{\text{t,max}}}{\Delta i_{\text{b,max}} + \Delta i_{\text{t,max}}} i^2_{L_\mu,\text{pk}}}} \tag{56}$$

The result of (56) can be substituted into (46) and (43) to determine the remaining inductance values. Note that as the calculation of (56) employs the tight coupling approximation, the exact effective resonant inductances should be used in (55) to size the bypass capacitor and ensure that the desired value of $\Gamma_{\min}$ is attained.

2) LIMITATIONS OF LINEAR COMPONENT SELECTION

Though the linear model provides closed form expressions for the CSBC component values, it has several disadvantages for selecting components in practical converters. Various assumptions must be satisfied to apply linear component selection, particularly for C-CSBCs. To ensure that second-order ripple effects are minimal, designers must arbitrarily choose a large value of $\Gamma_{\min}$, which can result in an oversized bypass capacitor. At the same time, the linear charge model is often inaccurate for determining capacitor voltage ripple, so it is also possible for the bypass capacitor to be undersized by linear component selection. Additionally, linear component selection is not easily applicable to C-CSBCs, and even after applying significant approximation, the equations for the optimal component values remain cumbersome.

B. DESIGN EXAMPLE

In contrast to linear component selection, the proposed models in Sections II and III do not require a high value of $\Gamma_{\min}$ for accuracy, but lack closed form equations to select the component values. Instead, methods such as numerical optimization are required to pick the passive components. A design example is presented here, comparing the components selected with the conventional linear approach to those found by numerical optimization with the model developed in this work. The converter is designed based on the specifications in Table 5. Based on the results of Fig. 15, a wide-range, CC load case is chosen to provide an example where coupling reduces overall component volume.

Table 6 shows component values for the coupled and uncoupled designs. The value of $\Gamma_{\min}$ used for the linear approach in existing literature varies from 11.6 to 47.9 [1], [11]. Therefore, $\Gamma_{\min} = 10$ is chosen for the linear component design to provide an optimistic comparison. The component energy densities are selected for a conservative capacitive-to-magnetic energy density ratio $\rho_{\text{E,C}}/\rho_{\text{E,L}} = 100$ [45].

TABLE 5. CSBC Design Example Specifications

Specification	Value
V_{in}	20 V
I_{load}	10 A
f_{sw}	100 kHz
D	[0.2, 0.8]
$\rho_{\text{E,L}}$	100 μJ/cm^3
$\rho_{\text{E,C}}$	10 mJ/cm^3
$\Delta i_{\text{t,max}}$	2.4 A
$\Delta i_{\text{b,max}}$	2.4 A
$v_{C_{\text{b}},\text{max}}$	30 V

TABLE 6. Design Example Component Values and Required Volumes Selected Using Numerical Optimization and Linear Approach With $\Gamma_{\min} = 10$ for Uncoupled and Coupled Inductor CSBCs

Uncoupled Passive Components

	Numerical (this work)	Linear
L_{t}	20.8 μH	20.8 μH
L_{b}	20.8 μH	20.8 μH
C_{b}	1.8 μF	12.2 μF
Volume	16 cm^3	16.3 cm^3

Coupled Passive Components

	Numerical (this work)	Linear
L_μ	9.97 μH	9.13 μH
$L_{\ell t}$	0.899 μH	2.57 μH
$L_{\ell b}$	0.899 μH	2.57 μH
C_{b}	15.5 μF	55.4 μF
Volume	8.69 cm^3	10.1 cm^3

For the given specifications, the best-case reduction in magnetic component volume $\varphi_{\text{c}} = 0.5$ is found by applying (54). This indicates a significant decrease in magnetic component volume is attainable by coupling, suggesting that the optimized C-CSBC should utilize a tightly coupled inductor. Based on the analysis in Section IV, a substantial increase in bypass capacitance is therefore required to compensate for the reduced effective resonant inductances which result from tight coupling. This aligns with the numerically optimized component values shown in Table 6, with the C-CSBC employing a high coupling coefficient $k = 0.92$ and bypass capacitance over 8 times larger than for the U-CSBC. The C-CSBC achieves a 45.6% decrease in overall passive volume, due to the magnetic components occupying the majority of the volume.

In both the uncoupled and coupled designs, the bypass capacitor selected by the linear approach is significantly larger than the numerically optimized bypass capacitor. In the uncoupled implementation, the volume required from the linear selection method is only slightly increased, as the capacitor volume is minimal. In contrast, for the coupled design, the

TABLE 7. **U-CSBC Experimental Input Passive Components. Total Component Box Volume: 11.5 cm³.**

Component	Description	Parameters	Image
L_t, L_b	Windings: 12 AWG 16 Core: TDK RM8 Ferrite (B65811J0000R049) Gap: 0.356 mm	$L_t = 20.5\ \mu$H $L_b = 20.1\ \mu$H Box Volume (Total) $= 11.5$ cm^3	
C_b	KEMET MLCC (C1206C475K5RACAUTO) Case: 1206	$C_b(20\text{ V}) = 1.5\ \mu$F Box Volume $= 0.00922$ cm^3	

TABLE 8. **C-CSBC Experimental Input Passive Components. Total Component Box Volume: 5.9 cm³.**

Component	Description	Parameters	Image
Coupled Inductor	Windings: 2x9 AWG 18 Core: TDK RM8 Ferrite (B65811J0000R049) Gap: 0.356 mm	$L_{\ell t} = 0.784\ \mu$H $L_{\ell b} = 0.849\ \mu$H $L_\mu = 10.7\ \mu$H Box Volume $= 5.75$ cm^3	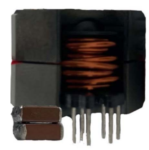
C_b	2x KEMET MLCC (C2220C156K5RACTU) Case: 2220	$C_b(20\text{ V}) = 20.2\ \mu$F Box Volume (Total) $= 0.145$ cm^3	

volume for the linear approach is noticeably larger than for the numerically selected components, as the capacitor occupies a considerable volume. From a passive volume perspective, careful design of the bypass capacitor is most important when its volume is relatively large. For C-CSBCs, proper sizing of the bypass capacitor is particularly important, as its volume is increased with tighter coupling. However, reducing the bypass capacitance can be beneficial for other reasons, such as lower cost and enabling the use of smaller packages with reduced ESL [46]. Finally, in many applications it should be considered that the value of $\Gamma_{\min}$ as well as coupling strength impacts the small-signal behavior of the converter which is not addressed in this work [1], [11].

VI. EXPERIMENTAL RESULTS

To validate the proposed model and the potential to reduce component volume by coupling, a testbed was built as shown in Fig. 16. Experimental results were obtained using a converter designed for the specifications provided in Table 5. Passive components were selected based on the numerically optimized component values found in Table 6. The components used and their box volumes for the uncoupled and coupled CSBC implementations are provided in Tables 7 and 8 respectively. Fig. 17 compares the modeled and measured output voltage as $\Gamma_1 \approx \Gamma_2$ increases from around resonance to above resonance. For the coupled inductors designed here, the leakage inductance is much smaller than the magnetizing inductance, resulting in a high coupling coefficient of $k = 0.93$. The C-CSBC converges to the nominal voltage conversion ratio at a lower $\Gamma_{\min}$, aligning with the results from Fig. 12. Plots of the modeled and measured inductor current and bypass capacitor voltage waveforms are provided for $D \in \{0.2, 0.5, 0.8\}$ in Figs. 18–20. These duty cycles are chosen as all maximum ripples, peak inductor currents, and peak bypass capacitor voltage occur at one of these duty cycles. The experimental waveforms closely match the modeled waveforms, though some error exists due to losses, which are not considered in the proposed model. Loss results in damping of resonant behavior, and dc offset in the capacitor voltage due to source resistance. In the coupled case, the lowered effective resonant inductances amplify the effects of damping, and the oversized capacitor lowers voltage ripple, making both forms of error more noticeable.

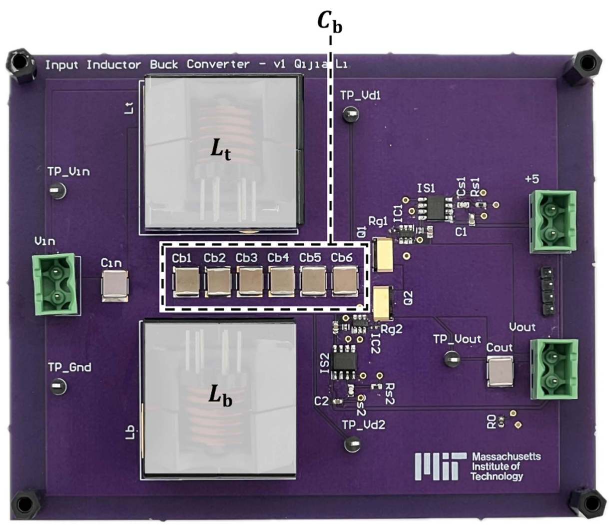

FIGURE 16. **Experimental testbed of the CSBC. The L_t, L_b and C_b shown on the testbed indicate component placement only. The actual components used for testing and their detailed parameters are given in Tables 7 and 8.**

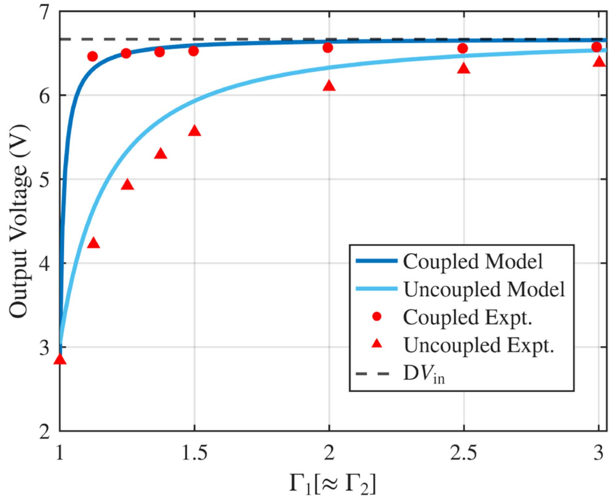

FIGURE 17. Output voltage measurement with varying switching frequencies.

In the uncoupled design, the effective energy densities were $\rho_{L_t,\text{eff}} = 139.5\ \mu\text{J/cm}^3$, $\rho_{L_b,\text{eff}} = 133.5\ \mu\text{J/cm}^3$ and $\rho_{C_b,\text{eff}} = 65.15\ \text{mJ/cm}^3$. In the coupled design, the effective energy densities were $\rho_{L,\text{eff}} = 142.6\ \mu\text{J/cm}^3$ and $\rho_{C_b,\text{eff}} = 28.87\ \text{mJ/cm}^3$. Thus, the magnetic components in the C-CSBC and U-CSBC achieve comparable effective energy densities, but the overall component volume is reduced by 48.7% in the C-CSBC. Despite the significant passive component volume reduction in the C-CSBC, the peak-to-peak current ripples of both implementations closely match at all maximum-stress duty cycles, indicating that coupling is directly responsible for the reduced component volume in the C-CSBC. Nonlinear behavior of the current waveforms is observed in both phases for the C-CSBC, matching the proposed model and producing dissimilar waveforms despite comparable peak-to-peak ripples between the uncoupled and coupled designs. In addition, as the C-CSBC bypass capacitor must be oversized due to the high inductor coupling coefficient, the switch stress of the C-CSBC is reduced. As a result, choosing between a C-CSBC and U-CSBC may also influence switch selection.

Notably, the effective capacitive energy density is significantly reduced in the coupled case. The capacitors were chosen for the same maximum voltage rating to account for ringing and derating, but the utilization of the oversized capacitor in the coupled design is lowered. Therefore, designers should consider that as tightly coupled C-CSBCs tend to require oversized bypass capacitors, it is likely that the capacitor utilization will be reduced compared to U-CSBCs. Nevertheless, the capacitor energy density was much higher than the magnetic component density in either design (over 400 and 200 times larger for the uncoupled and coupled designs respectively). Finally, the selection of component values could be further optimized by updating the method of Section V with the observed capacitive-to-magnetic energy density ratios.

VII. CONCLUSION

This paper presents a comprehensive analysis of the CSBC, applicable across various operating conditions and component parameters, including coupling between the two input inductors. The proposed model accurately characterizes the effects of the bypass capacitor on switch stress, resonant behavior in the input passive network, and output voltage regulation. The effects of coupling on passive volume requirements are thoroughly analyzed, demonstrating the possibility for coupling to directly reduce CSBC magnetic component volume under certain operating conditions, at the cost of decreasing the effective resonant inductances. An equivalence between coupling and output inductance is derived in Appendix A and B, providing intuition for the effects of coupling in a CSBC, and extending the analysis of coupling to comparison between CSBCs and conventional buck converters. Experimental results are provided to validate the accuracy of the proposed model and effectiveness of coupling in reducing passive component volume. Furthermore, this work establishes a foundation for analyzing other topologies with input inductor networks, extending its applicability to future topologies.

APPENDIX A
EQUIVALENCE OF COUPLING AND OUTPUT INDUCTANCE

The use of a coupled input inductor in a CSBC is electrically equivalent to the addition of an output inductor, as in a conventional buck converter. While an explicit derivation is provided here, the effect is not unique to the CSBC and has been explored for other topologies in existing literature [33], [34], [35]. Nevertheless, the "decoupled" model is valuable not only for providing further intuition into the effects of coupling in the CSBC, but also enables the analysis of the C-CSBC to be applied for comparison between CSBCs and conventional buck converters. To demonstrate this equivalence between coupling and output inductance, a general CSBC model with added output inductor L_o is shown in Fig. 21.

By inspection, it is clear that the current in L_o is given by $i_{L_o}(t) = i_{L_t}(t) + i_{L_b}(t)$ in either phase. Meanwhile, the voltages across L_t and L_b in phase one are given by KVL:

$$\begin{aligned} v_{L_t,1}(t) &= V_{in} - v_{L_o,1}(t) - V_{out} \\ v_{L_b,1}(t) &= -v_{L_o,1}(t) + v_{C_b,1}(t) - V_{out} \end{aligned} \tag{57}$$

In phase two, the corresponding inductor voltage equations are

$$\begin{aligned} v_{L_t,2}(t) &= V_{in} - v_{C_b,2}(t) - v_{L_o,2}(t) - V_{out} \\ v_{L_b,2}(t) &= -v_{L_o,2}(t) - V_{out} \end{aligned} \tag{58}$$

The input inductor voltage and output inductor current equations for the CSBC with output inductance are identical to their corresponding equations for the C-CSBC in Section III if $L_t = L_{\ell t}$, $L_b = L_{\ell b}$ and $L_o = L_\mu$.

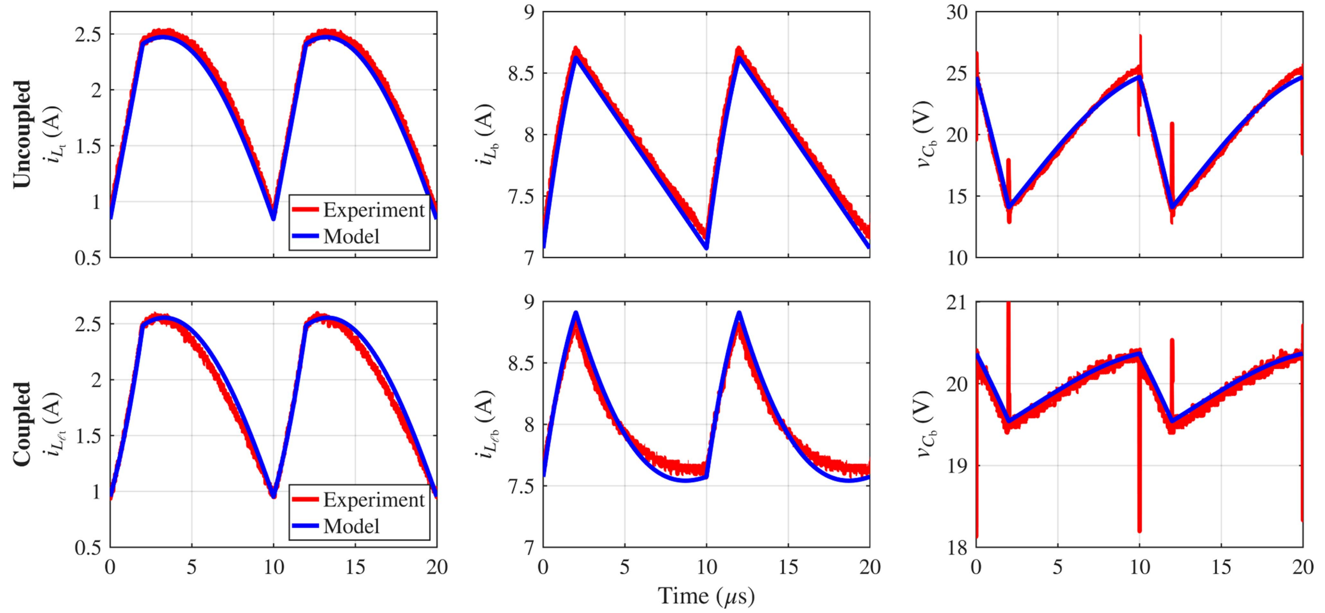

FIGURE 18. Experimental and modeled inductor current and bypass capacitor voltage waveforms for $D = 0.2$.

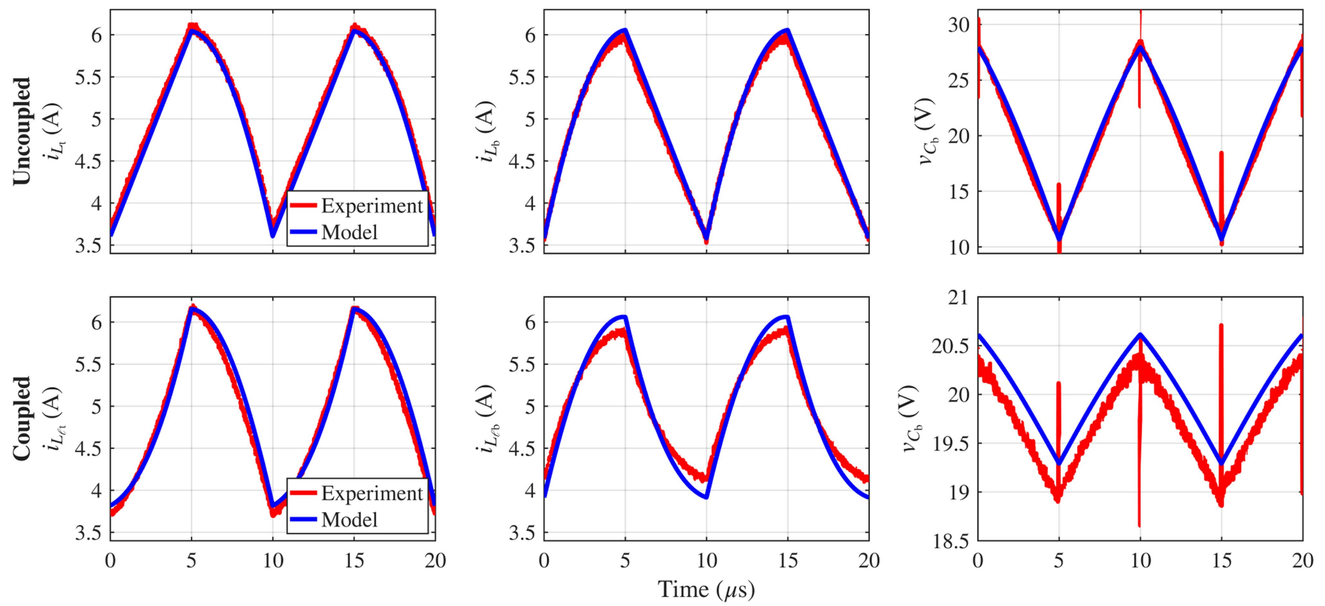

FIGURE 19. Experimental and modeled inductor current and bypass capacitor voltage waveforms for $D = 0.5$.

Furthermore, because the bypass capacitor current is equal to $-i_{L_b}(t)$ or $i_{L_t}(t)$ in phase one and two respectively, the bypass capacitor waveforms also match those of the C-CSBC. A unity turns ratio C-CSBC therefore provides the same electrical behavior as an U-CSBC with the addition of an output inductor equal to the coupled inductor magnetizing inductance, and input inductors equal to the leakage inductances. If $L_t = L_b = C_b = 0$, the output inductor CSBC becomes identical to a conventional buck converter.

APPENDIX B
COMPARISON BETWEEN CSBCS AND CONVENTIONAL BUCK CONVERTERS

Applying the equivalence between coupling and output inductance enables the analysis of C-CSBC volume in Section IV to be applied in comparing CSBCs with conventional output inductor buck converters. As the calculation of φ_c, the best-case reduction in magnetic energy storage requirements by coupling, assumes zero leakage inductance, the theoretical minimum magnetic component volume for a C-CSBC is

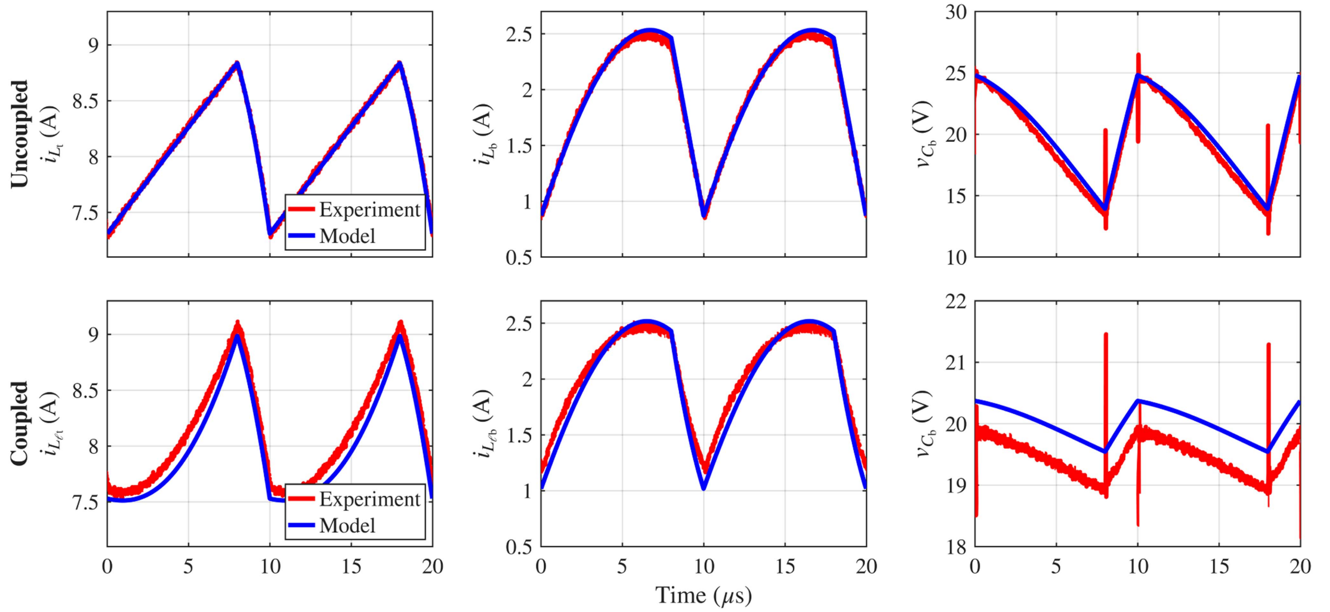

FIGURE 20. Experimental and modeled inductor current and bypass capacitor voltage waveforms for $D = 0.8$.

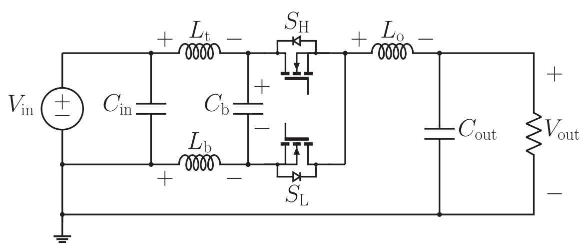

FIGURE 21. Electrically equivalent converter model for a C-CSBC, U-CSBC with added output inductance, or conventional buck converter with added input inductors.

the same as that of a conventional buck converter's output inductor. Thus, φ_{c} can also be interpreted as a first-order comparison between the magnetic component volumes of a conventional buck converter and the input inductors of a CSBC. The magnetic component volume and bypass capacitance comparison for conventional buck converters and CSBCs is summarized in Table 9.

It is also notable that in the case of the C-CSBC, it is not required that both leakage inductors are nonzero. In fact, in "ripple steering", $L_{\ell\text{b}} = 0$, which results in zero first-order input ripple. By inspection of Fig. 21, this is identical to a conventional buck converter with an LC input EMI filter, which has been described in [33]. In this special case, $L_{\ell\text{t}}$ acts purely as an input EMI filter inductor, and does not reduce output current ripple. In general, if bypass capacitor ripple is neglected, the output current ripple of a C-CSBC is the same as a conventional buck converter with output inductance $L_{\text{o,eq,c}} = L_{\ell\text{t}} \| L_{\ell\text{b}} + L_{\mu}$. For U-CSBCs, $L_{\mu} = 0$, resulting in $L_{\text{o,eq,u}} = L_{\text{t}} \| L_{\text{b}}$. Thus, while the behavior at the input of the CSBC is significantly altered compared to a conventional buck converter, the output behavior is unchanged, excepting second-order effects.

TABLE 9. Component Sizing Comparison Between Conventional Buck Converters and CSBCs, Assuming Constant Magnetic Energy Density and Operation Significantly Above Resonance. If $\varphi_{\text{c}} < 1$, Either Variant of CSBC Requires Increased Magnetic Component Volume Than a Conventional Buck Converter. C-CSBCs can Mitigate This Increased Magnetic Component Volume at the Cost of Requiring a Larger Bypass Capacitance Than U-CSBCs.

Topology	Normalized Vol_{mag}	Normalized C_{b}
Conventional	1	0
U-CSBC	$1/\varphi_{\text{c}}$	1
C-CSBC	$\left(\frac{L_{\text{x}}}{\varphi_{\text{c}}} + L_{\mu}\right) / (L_{\text{x}} + L_{\mu})$	$\leq 1/(1-k)$ $> 1/(1-k^2)$

REFERENCES

[1] W. W. Weaver and P. T. K. Krein, "Analysis and applications of a current-sourced buck converter," in *Proc. APEC 07-22nd Annu. IEEE Appl. Power Electron. Conf. Expo.*, 2007, pp. 1664–1670.

[2] Q. Li and S. Coday, "A general analysis of passive component sizing for input inductor buck converters," in *Proc. IEEE 26th Workshop Control Model. Power Electron.*, 2025, pp. 1–8.

[3] R. S. Bayliss and R. C. Pilawa-Podgurski, "An input inductor flying capacitor multilevel converter utilizing a combined power factor correcting and active voltage balancing control technique for buck-type AC/DC grid-tied applications," in *Proc. IEEE Workshop Control Model. Power Electron.*, 2024, pp. 1–7.

[4] W. C. Liu, T. Ge, and R. C. N. Pilawa-Podgurski, "A bi-lateral energy resonant conversion (BERC) technique for improved passive utilization in hybrid switched-capacitor converters," *IEEE Open J. Power Electron.*, vol. 3, pp. 772–786, 2022.

[5] A. K. Delmar and A. Stillwell, "Current-sourced hybrid switched-capacitor converter for data center power delivery," in *Proc. IEEE Appl. Power Electron. Conf. Expo.*, 2024, pp. 1357–1362.
[6] W. Vavrik, A. K. Delmar, and A. Stillwell, "Control and modeling of current-sourced hybrid switched-capacitor converters with dynamic loads," in *Proc. IEEE Workshop Control Model. Power Electron.*, 2024, pp. 1–7.
[7] C. Babu and M. Veerachary, "Predictive valley current controller for two inductor buck converter," in *Proc. IEEE Int. Symp. Circuits Syst.*, 2005, vol. 4 pp. 3075–3078.
[8] X. Ke, Z. Hay, and S. Tian, "Kappa switching DC-DC converter with continuous input and output currents achieving 86.7% input ripple suppression and 16dB peak EMI reduction," in *Proc. IEEE Appl. Power Electron. Conf. Expo.*, 2020, pp. 1315–1319.
[9] A. Abdulslam and P. P. Mercier, "8.2 a continuous-input-current passive-stacked third-order buck converter achieving 0.7 W/mm^2 power density and 94% peak efficiency," in *Proc. IEEE Int. Solid-State Circuits Conf.*, 2019, pp. 148–150.
[10] J. Leppäaho and T. Suntio, "Dynamic characteristics of current-fed superbuck converter," *IEEE Trans. Power Electron.*, vol. 26, no. 1, pp. 200–209, Jan. 2011.
[11] M. Karppanen, J. Arminen, T. Suntio, K. Savela, and J. Simola, "Dynamical modeling and characterization of peak-current-controlled superbuck converter," *IEEE Trans. Power Electron.*, vol. 23, no. 3, pp. 1370–1380, May 2008.
[12] C. R. Sullivan, B. A. Reese, A. L. F. Stein, and P. A. Kyaw, "On size and magnetics: Why small efficient power inductors are rare," in *Proc. Int. Symp. 3D Power Electron. Integration Manuf.*, 2016, pp. 1–23.
[13] K. Wang, S. Y. Sim, Y. Q. Choong, S. Pakala, X. Zhang, and C. Huang, "A high density three-level quadratic buck hybrid converter for 48V-to-pol conversion," in *Proc. IEEE Appl. Power Electron. Conf. Expo.*, 2025, pp. 505–509.
[14] K. Radhakrishnan, M. Swaminathan, and B. K. Bhattacharyya, "Power delivery for high-performance microprocessors—Challenges, solutions, and future trends," *IEEE Trans. Compon. Packag. Manuf. Technol.*, vol. 11, no. 4, pp. 655–671, Apr. 2021.
[15] A. Aron, P. Eliat-Eliat, J. Buonato, and S. Coday, "Analysis and design of a condensed buck–boost converter utilizing monolithic bidirectional GAN switches," *IEEE Trans. Power Electron.*, vol. 41, no. 1, pp. 1226–1240, Jan. 2026.
[16] A. Schellmanns, J.-P. Keradec, J.-L. Schanen, and K. Berrouche, "Representing electrical behaviour of transformers by lumped element circuits: A global physical approach," in *Proc. Conf. Rec. IEEE Ind. Appl. Conf. 34th IAS Annu. Meeting*, 1999, vol. 3, pp. 2100–2107.
[17] J. Li, C. Sullivan, and A. Schultz, "Coupled-inductor design optimization for fast-response low-voltage DC-DC converters," in *Proc. APEC. 17th Annu. IEEE Appl. Power Electron. Conf. Expo.*, 2002, vol. 2, pp. 817–823.
[18] J. G. Kassakian, D. J. Perreault, G. C. Verghese, and M. F. Schlecht, *Principles of Power Electronics*. Cambridge, U.K.: Cambridge Univ. Press, 2024.
[19] P. Holenarsipur, N. Mohan, V. Albertson, and J. Cristofersen, "Avoiding the use of negative inductances and resistances in modeling three-winding transformers for computer simulations," in *Proc. IEEE Power Eng. Soc. Winter Meeting*, 1999, vol. 2, pp. 1025–1030.
[20] B. Hauke, "Basic calculation of a boost converter's power stage," Texas Instruments Incorporated, Application Note SLVA372D, Nov. 2022. [Online]. Available: https://www.ti.com/lit/an/slva372d/slva372d.pdf
[21] F. Dostal, "Selecting the right inductor current ripple," Technical Article on Analog Devices Website, Mar. 2023. Accessed: Jan. 20, 2026. [Online]. Available: https://www.analog.com/en/resources/technical-articles/selecting-the-right-inductor-current-ripple.html
[22] A. Arif, Z. Wang, J. Wang, B. Mather, H. Bashualdo, and D. Zhao, "Load modeling—A review," *IEEE Trans. Smart Grid*, vol. 9, no. 6, pp. 5986–5999, Nov. 2018.
[23] F. de León, S. Purushothaman, and L. Qaseer, "Leakage inductance design of toroidal transformers by sector winding," *IEEE Trans. Power Electron.*, vol. 29, no. 1, pp. 473–480, Jan. 2014.
[24] A. Sharma and J. W. Kimball, "Transformer leakage inductance design methodology," in *Proc. IEEE Appl. Power Electron. Conf. Expo.*, 2023, pp. 1572–1578.
[25] W. Hurley and D. Wilcox, "Calculation of leakage inductance in transformer windings," *IEEE Trans. Power Electron.*, vol. 9, no. 1, pp. 121–126, Jan. 1994.
[26] M. Li, Z. Ouyang, and M. A. E. Andersen, "High-frequency LLC resonant converter with magnetic shunt integrated planar transformer," *IEEE Trans. Power Electron.*, vol. 34, no. 3, pp. 2405–2415, Mar. 2019.
[27] S. Ć UK and Z. Zhang, "Coupled-inductor analysis and design," in *Proc. 17th Annu. IEEE Power Electron. Specialists Conf.*, 1986, pp. 655–665.
[28] D. Choi, S. Baek, Y. Cho, S.-J. Yeo, and H. Kim, "Design of coupled inductor considering saturation of core by leakage inductance for a 100kW interleaved inverter," in *Proc. 10th Int. Conf. Power Electron. ECCE Asia*, 2019, pp. 2814–2819.
[29] Y. Cai et al., "Magnetic integration for a dual active bridge converter planar transformer with accurate leakage inductances estimation," *IEEE Access*, vol. 12, pp. 112278–112289, 2024.
[30] S. Cuk, "Switching DC-to-DC converter with zero input or output current ripple," in *Proc. IEEE Ind. Appl. Soc. Annu. Meeting*, 1978, pp. 1131–1146.
[31] M. Brkovic and S. Cuk, "Input current shaper using Cuk converter," in *Proc. 14th Int. Telecommun. Energy Conf. - INTELEC '92*, 1992, pp. 532–539.
[32] R. S. Balog and P. T. Krein, "Coupled-inductor filter: A basic filter building block," *IEEE Trans. Power Electron.*, vol. 28, no. 1, pp. 537–546, Jan. 2013.
[33] J. Kolar, H. Sree, N. Mohan, and F. Zach, "Novel aspects of an application of 'zero'-ripple techniques to basic converter topologies," in *Proc. PESC97. Rec. 28th Annu. IEEE Power Electron. Specialists Conf. Formerly Power Conditioning Specialists Conf. 1970-71. Power Process. Electron. Specialists Conf.*, 1972, vol. 1, pp. 796–803.
[34] D. Hamill and P. Krein, "A 'zero' ripple technique applicable to any DC converter," in *Proc. 30th Annu. IEEE Power Electron. Specialists Conf. Record.*, 1999, vol. 2, pp. 1165–1171.
[35] E. Landsman, "A unifying derivation of switching DC-DC converter topologies," in *Proc. IEEE Power Electron. Specialists Conf.*, 1979, pp. 239–243.
[36] H. N. Nagaraja, D. Kastha, and A. Petra, "Design principles of a symmetrically coupled inductor structure for multiphase synchronous buck converters," *IEEE Trans. Ind. Electron.*, vol. 58, no. 3, pp. 988–997, Mar. 2011.
[37] G. Zhu and K. Wang, "Modeling and design considerations of coupled inductor converters," in *Proc. 25th Annu. IEEE Appl. Power Electron. Conf. Expo.*, 2010, pp. 7–13.
[38] G. Zhu, B. A. McDonald, and K. Wang, "Modeling and analysis of coupled inductors in power converters," *IEEE Trans. Power Electron.*, vol. 26, no. 5, pp. 1355–1363, May 2011.
[39] P. Dowell, "Effects of eddy currents in transformer windings," *Proc. Inst. Elect. Eng.*, vol. 113, pp. 1387–1394, 1966. [Online]. Available: https://digital-library.theiet.org/doi/abs/10.1049/piee.1966.0236
[40] X. Nan and C. Sullivan, "Simplified high-accuracy calculation of eddy-current loss in round-wire windings," in *Proc. IEEE 35th Annu. Power Electron. Specialists Conf.*, 2004, vol. 2, pp. 873–879.
[41] J. Ferreira, "Improved analytical modeling of conductive losses in magnetic components," *IEEE Trans. Power Electron.*, vol. 9, no. 1, pp. 127–131, Jan. 1994.
[42] J. Muhlethaler, J. Biela, J. W. Kolar, and A. Ecklebe, "Core losses under the DC bias condition based on steinmetz parameters," *IEEE Trans. Power Electron.*, vol. 27, no. 2, pp. 953–963, Feb. 2012.
[43] C. A. Baguley, B. Carsten, and U. K. Madawala, "The effect of DC bias conditions on ferrite core losses," *IEEE Trans. Magn.*, vol. 44, no. 2, pp. 246–252, Feb. 2008.
[44] M. Mu, F. Zheng, Q. Li, and F. C. Lee, "Finite element analysis of inductor core loss under DC bias conditions," *IEEE Trans. Power Electron.*, vol. 28, no. 9, pp. 4414–4421, Sep. 2013.
[45] N. C. Brooks, J. Zou, S. Coday, T. Ge, N. M. Ellis, and R. C. N. Pilawa-Podgurski, "On the size and weight of passive components:scaling trends for high-density power converter designs," *IEEE Trans. Power Electron.*, vol. 39, no. 7, 2024, pp. 8459–8477, Jul. 2024.
[46] Y. Ding, F. Squires, S. Lee, A. E. Ruehli, and C. Hwang, "Comprehensive measurement and cross-sectional study of decoupling capacitor interconnect inductance," *IEEE Trans. Signal Power Integrity*, vol. 4, pp. 46–54, 2025.

QIJIA LI (Graduate Student Member, IEEE) received the B.S. degree in electrical and computer engineering from Cornell University, Ithaca, NY, USA, in 2023 and the M.S. degree in electrical engineering and computer science in 2026, from the Massachusetts Institute of Technology, Cambridge, MA, USA, where she is currently working toward the Ph.D. degree with a focus on power electronics.

JONAH RAWLEY (Graduate Student Member, IEEE) received the B.E.E. degree from the University of Minnesota - Twin Cities, Minneapolis, MN, USA, in 2025. He is currently working toward the Ph.D. degree with the Massachusetts Institute of Technology, Cambridge, MA, USA, with a research focus in power electronics.

SAMANTHA CODAY (Member, IEEE) received the B.S. degree in electrical engineering and mathematics from Southern Methodist University, Dallas, TX, USA, in 2017, and the M.S. degree and Ph.D. degree in electrical engineering and computer sciences from the University of California, Berkeley, CA, USA, in 2019 and 2023, respectively. In 2023, she joined the Massachusetts Institute of Technology, as an Assistant Professor of electrical engineering. She is currently the Emanuel E. Landsman (1958) Career Development Assistant Professor of electrical engineering with the Massachusetts Institute of Technology, Cambridge, MA, USA. Her research interests include hybrid switched-capacitor circuits focusing on the design and implementation of converters in future electrified transportation, grid-tied conversion, and data center power delivery. Dr. Coday was the recipient of the ARPA-E IGNIITE Young Investigator and the NSF CAREER awards.